NASA TECHNICAL NOTE

N73-33148

NASA TN D-7276

NASA TN D-7276

CASE FILE COPY

EVALUATION OF CONTROL LAWS AND ACTUATOR LOCATIONS FOR CONTROL SYSTEMS APPLICABLE TO DEFORMABLE ASTRONOMICAL TELESCOPE MIRRORS

by Aaron J. Ostroff

Langley Research Center
Hampton, Va. 23665

NATIONAL AERONAUTICS AND SPACE ADMINISTRATION • WASHINGTON, D. C. • OCTOBER 1973

1. Report No.	2. Government Accession No.	3. Recipient's Catalog No.
NASA TN D-7276		

4. Title and Subtitle	5. Report Date
EVALUATION OF CONTROL LAWS AND ACTUATOR LOCATIONS FOR CONTROL SYSTEMS APPLICABLE TO DEFORMABLE ASTRONOMICAL TELESCOPE MIRRORS	October 1973
	6. Performing Organization Code
7. Author(s)	8. Performing Organization Report No.
Aaron J. Ostroff	L-8862
	10. Work Unit No.
9. Performing Organization Name and Address	188-78-57-07
NASA Langley Research Center Hampton, Va. 23665	11. Contract or Grant No.
	13. Type of Report and Period Covered
12. Sponsoring Agency Name and Address	Technical Note
National Aeronautics and Space Administration Washington, D.C. 20546	14. Sponsoring Agency Code

15. Supplementary Notes

16. Abstract

Some of the major difficulties associated with large orbiting astronomical telescopes are the cost of manufacturing the primary mirror to precise tolerances and the maintaining of diffraction-limited tolerances while in orbit. One successfully demonstrated approach for minimizing these problem areas is the technique of actively deforming the primary mirror by applying discrete forces to the rear of the mirror. A modal control technique, as applied to active optics, has previously been developed and analyzed. The modal control technique represents the plant to be controlled in terms of its eigenvalues and eigenfunctions which are estimated via numerical approximation techniques.

This paper includes an extension of previous work using the modal control technique and also describes an optimal feedback controller. The equations for both control laws are developed in state-space differential form and include such considerations as stability, controllability, and observability. These equations are general and allow the incorporation of various mode-analyzer designs; two design approaches are presented. This paper also includes a technique for placing actuator and sensor locations at points on the mirror based upon the flexibility matrix of the uncontrolled or unobserved modes of the structure. The locations selected by this technique are used in the computer runs which are described. The results are based upon three different initial error distributions, two mode-analyzer designs, and both the modal and optimal control laws.

17. Key Words (Suggested by Author(s))	18. Distribution Statement
Astronomical telescope Active optics Modal control	Unclassified – Unlimited

19. Security Classif. (of this report)	20. Security Classif. (of this page)	21. No. of Pages	22. Price*
Unclassified	Unclassified	62	Domestic, $3.50 Foreign, $6.00

*For sale by the National Technical Information Service, Springfield, Virginia 22151

Page Intentionally Left Blank

CONTENTS

	Page
SUMMARY	1
INTRODUCTION	1
SYMBOLS	4
MODAL CONTROL TECHNIQUE	7
DEVELOPMENT OF OPTIMAL CONTROLLER	14
STABILITY, CONTROLLABILITY, AND OBSERVABILITY	17
SELECTION OF ACTUATOR AND SENSOR LOCATIONS	19
DESIGNING THE MODE ANALYZER	22
CONTROL-SYSTEM COMPUTER RESULTS	25
CONCLUDING REMARKS	29
APPENDIX A – SPECIAL PROPERTIES OF CONTROL LAWS	31
I. Stability	31
Modal control law	31
Optimal control law	32
II. Selection of the Force-Transformation Compensation Matrix	32
Modal control law	32
Optimal control law	33
III. Equal Number of Actuators and Sensors	33
Modal control law	34
Optimal control law	34
REFERENCES	37
FIGURES	38

EVALUATION OF CONTROL LAWS AND ACTUATOR LOCATIONS FOR CONTROL SYSTEMS APPLICABLE TO DEFORMABLE ASTRONOMICAL TELESCOPE MIRRORS

By Aaron J. Ostroff
Langley Research Center

SUMMARY

Some of the major difficulties associated with large orbiting astronomical telescopes are the cost of manufacturing the primary mirror to precise tolerances and the maintaining of diffraction-limited tolerances while in orbit. One successfully demonstrated approach for minimizing these problem areas is the technique of actively deforming the primary mirror by applying discrete forces to the rear of the mirror. A modal control technique, as applied to active optics, has previously been developed and analyzed. The modal control technique represents the plant to be controlled in terms of its eigenvalues and eigenfunctions which are estimated via numerical approximation techniques.

This paper includes an extension of previous work using the modal control technique and also describes an optimal feedback controller. The equations for both control laws are developed in state-space differential form and include such considerations as stability, controllability, and observability. These equations are general and allow the incorporation of various mode-analyzer designs; two design approaches are presented. This paper also includes a technique for placing actuator and sensor locations at points on the mirror based upon the flexibility matrix of the uncontrolled or unobserved modes of the structure. The locations selected by this technique are used in the computer runs which are described. The results are based upon three different initial error distributions, two mode-analyzer designs, and both the modal and optimal control laws.

INTRODUCTION

There are many advantages to operating a large telescope outside the Earth's atmosphere. The increased resolution and expanded transmission range will allow a greater exploration of the universe over that which is possible from Earth. However, major difficulties are involved in the large cost of manufacturing the primary mirror and in technical problems associated with maintaining diffraction-limited performance despite such factors as gravity release, temperature gradients across and through the mirror, initial fabrication errors, and various induced stresses resulting from the telescope structure.

One proposed solution which greatly reduces the initial fabrication cost and maintains diffraction-limited tolerances is to control actively the figure of the primary mirror. The first experimental attempt to demonstrate the feasibility of active figure-error control was to maintain the three segments of a 0.5-meter-diameter spherical mirror in precise relationship to each other (ref. 1). Although this approach was successful for the small mirror used, the construction of large off-axis aspheric segments matched in focal length to diffraction-limited tolerances was beyond the technical state of the art.

A more advanced approach to active figure-error control is to deform a flexible mirror to the desired figure by applying forces at discrete points on the rear of a primary mirror by means of actuators (fig. 1). An optical figure-error sensor scans the mirror and generates signals proportional to the deformations from the nominal figure. These signals are processed by a controller which in turn feeds appropriate signals to the actuators.

A modal control technique, which describes the behavior of the mirror and its supporting structure by its eigenvalues (frequencies) and eigenfunctions (mode shapes), has been developed by Creedon and Lindgren (ref. 2) for application to large orbiting telescope primary mirrors. This technique was applied to distributed parameter plants where the eigenvalues and eigenfunctions have closed-form solutions. For typical telescope applications with complex mirror mounts, a central hole in the primary mirror, and actuator masses at the rear of the mirror, numerical approximation techniques are required to analyze the dynamics. A structural analysis program using numerical techniques was used by Howell and Creedon (ref. 3) to analyze a 1-meter-diameter, solid homogeneous spherical mirror for application to the active optics modal control loop. Reference 3 contains an explanation of the control system and a design procedure based upon use of the modal control technique. Two approaches for treatment of initial errors are presented; the first approach is deterministic for treatment of known or expected errors, whereas the second approach assumes uncorrelated errors for cases where the disturbances are unknown. The latter approach was found to be less sensitive to variations in error distribution and was preferred even though it requires more actuators than the deterministic method for a specific error. Further, for the uncorrelated treatment of errors, a technique is shown to estimate the number of actuators required to reduce the initial error by a predetermined amount. The location of actuators will be near the common node lines of the most predominant uncontrolled modes.

Simultaneous with the theoretical work, laboratory experimentation on a 1-meter-diameter spherical mirror was being done to demonstrate the feasibility of this approach (refs. 4 and 5). Investigation of a few control laws showed that the modal control law requires the fewest actuators to reach the desired performance index (ref. 4).

Although the groundwork for active figure-error control has been established, several areas of investigation remain. Previous theoretical work assumes perfect estimates of the modal-displacement coefficients, and sensor locations always include actuator locations as a subset. The technique for selecting actuator locations requires an exhaustive computer search of the areas near common node lines of the most predominant uncontrolled modes. For higher order modes, this technique becomes very time consuming and costly.

The analysis and computer results described in this paper is an extension of the work summarized previously and attempts to improve upon the deficiencies described. Since the main purpose of this work is to evaluate the steady-state error of the control system as a function of the number and location of actuator and sensor points, the control equations are derived in a very general form and allow any number and any location of actuators and figure sensors. An improved technique for selecting actuator and figure-error sensor locations includes the effect of all uncontrolled or unobserved modes. The technique is essentially computerized, requires relatively little time, and is relatively inexpensive as compared with the search techniques used previously.

The numerical analyses used for this paper allow 250 locations for actuators and sensors, as opposed to 58 locations for the previous references. Both the mode analyzer and the force-compensation transformation matrix (described in the section entitled "Modal Control Technique") are included in a general form to allow evaluation of different designs. Previous work assumes only one particular case. A feedback optimal control law, defined as the least squares fit to the desired shape, is developed for comparison with the modal control law. For the analysis in this paper, the performance index is chosen as the rms error of the mirror surface.

The first section of this paper discusses the modal control technique and includes a brief description of the structural model used to calculate the eigenvalues and eigenfunctions of the mirror, a description of the modal control loop and all of its components, and a complete development of the state-space differential equations describing the system. The steady-state solution to these differential equations is given for a step-input disturbance. Finally, a performance index is defined as the rms error of the mirror surface.

The second section includes the development of a feedback optimal control law, which is the least squares fit to desired shape. This approach uses all of the estimated modal-displacement coefficients and weights them by their corresponding eigenvalues and eigenvectors. This controller is integrated into the control system, and the state-space differential equations describing the control system are developed.

The third section of this paper considers stability, state and output controllability, and observability for both the modal and optimal control laws.

The fourth section describes a technique for selecting actuator and figure-error sensor locations. This technique is based upon minimizing that part of the potential energy which is in the uncontrolled modes. In order to minimize the work involved, an approximate selection technique is described that is essentially computerized, but requires the designer to select locations from contour plots. Suggested locations for 4, 7, 10, 15, and 20 actuators or sensors are shown.

The control-system equations are very general and allow the incorporation of any mode-analyzer design; two designs are described in the fifth section. For each design, special properties of the coefficient transition matrices are described.

The least expensive and most flexible approach for design and evaluation of an active-optics control system is by computer simulation. Various numbers and different locations of actuators and figure-error sensors along with different control laws and mirror configurations can be easily evaluated. The sixth section of this paper describes the control-system computer results for a 0.762-meter-diameter mirror with a 60-to-1 ratio of diameter to thickness and a radius of curvature of 4.52 meters. Results from several computer runs are shown for three different initial-error distributions and include two different mode-analyzer designs and both the modal and optimal control laws. Some special properties of the two control laws are given in appendix A.

SYMBOLS

A	coefficient transition matrix (see eq. (19))
a	actuator force (modal coordinates)
B	control matrix for external disturbance (see eq. (19))
C	modal-displacement vector
$\hat{C}$	estimated modal-displacement vector
D	dynamic compensation matrix
E	output matrix (see eqs. (20))
F	control matrix (see eq. (19))
G	transmission matrix (see eqs. (20))
H	force-transformation matrix

H_e	force-transformation compensation matrix
I	identity matrix
I_p	potential energy
I_{pu}	potential energy in the uncontrolled modes
J	performance index
K	stiffness matrix
L	control matrix (see eq. (31))
M	total number of modes carried in the analysis
M_m	mass matrix
N	total number of mirror displacements observed and total number of modes sensed
n	number of controlled modes
P_{obn}	observability matrix for n controlled modes
P_{obr}	observability matrix for r modes observed in addition to those controlled
P_{oc}	output controllability matrix
P_{sc}	state controllability matrix
p	total number of modes carried in the analysis other than those controlled
Q	rms error remaining
q	external disturbance vector
R	remaining modes carried in the analysis that are neither controlled nor observed

r	number of modes observed in addition to those controlled
S	coefficient transition matrix (see eq. (31))
T	flexibility matrix
U	eigenvector matrix
U_e	mode-analyzer matrix
V	transfer function (see eqs. (13))
W	physical mirror displacements
X	state variable vector
X_{ss}	steady-state value of state variable vector
$\dot{X}$	differential of state variable vector
Y	external reference vector
Z	control matrix for external disturbances (see eq. (31))
α	actuator force (physical coordinates)
Λ	eigenvalue matrix

Superscripts:

Single letter	column vector with dimension of letter
Double letter	matrix denoting rows and columns, respectively
T	transpose
$*$	conjugate transpose
-1	inverse

MODAL CONTROL TECHNIQUE

In this section the finite-element structural model used to calculate the eigenvalues and eigenvectors of the mirror is described first and then the equations describing the modal control system are developed in state-space differential-equation form for comparison with an optimal control technique described in the next section. The equations are very general, allowing both the incorporation of any number and location of actuators and figure-error sensor points and the evaluation of different mode-analyzer and force-compensation transformation matrices.

The NASTRAN structural analysis program (ref. 6) has been used to calculate the eigenvalues and eigenvectors that are needed to model the mirror for control-system analysis. The finite-element structural model used in the structural analysis is shown in figure 2 and consists of 253 grid points and 462 triangular elements. All elements are homogeneous, include both membrane and bending effects, and, except for those elements on the exterior boundary, are equilateral triangles for best numerical accuracy. The numbering system used in the analysis was chosen to minimize the bandwidth of the stiffness and mass matrices for minimum storage and solution times (ref. 6). Grid points 15, 119, and 247 are the locations of a 3-point kinematic mount; grid point 15 is constrained in all three directions; grid point 247 is constrained only in the out-of-plane direction; and grid point 119 is constrained in the out-of-plane direction and in an in-plane direction that is perpendicular to the line joining grid points 119 and 135. The kinematic mount is a typically chosen support since the mirror is not overconstrained.

A block diagram of the modal control loop containing a mathematical model of the mirror, a figure-error sensor, and a controller is shown in figure 3. The vectors and matrices shown in this figure and throughout this paper are denoted by symbols with superscripts. A symbol with a single superscript represents a column vector with the dimension defined by the superscript, and a matrix is defined by a symbol with two superscripts denoting the row and column dimensions, respectively. The mirror is represented by a box which has α^n actuator forces acting on it and W^M finite-displacement outputs at M preselected locations. The three channels in this box represent: (1) the n controlled modes which are also equal to the number of actuators, (2) the r modes observed in addition to the controlled modes which are also observed, and (3) the R remaining modes carried in the numerical analysis that are neither observed nor controlled. In the modal representation of the mirror the actuator forces are first transformed from physical to modal coordinates by the force-transformation matrices and then weighted by the eigenvalues of the mirror and its supporting structure. For analysis in this paper, the eigenvalues and eigenvectors have been determined by the NASTRAN structural analysis program (ref. 6), and the eigenvalue matrices are inverses of those described in references 2 and 3. The outputs from the three eigenvalue matrix boxes are summed with the

q^M external modal mirror-displacement disturbances to form the C^M actual mirror displacements in modal coordinates where

$$M = n + r + R \tag{1}$$

with M being the total number of modes carried in the numerical analysis. The modal-displacement coordinates are transformed to the W^M physical-displacement coordinates by the displacement transformation matrix U^{MM}, which is the matrix of mode shapes of the mirror, as

$$W^M = U^{MM}C^M \tag{2}$$

The optical figure-error sensor observes N of the M physical mirror displacements ($N \leqq M$) and inputs proportional signals to the controller for processing. Although the C^M coefficients are mathematically obtainable, only the estimated modal-displacement coefficients $\hat{C}^N$ can be measured in a physical control system. The $\hat{C}^N$ vector may be calculated by using the mode analyzer $\left[U_e^{NN}\right]^{-1}$ which is also a coordinate transformation matrix between the physical and modal domains where

$$N = n + r \tag{3}$$

For the modal control technique, only the $\hat{C}^n$ vector is used for control. Later in this paper, an optimal controller is described which uses all of the estimated modal-displacement coefficients. The n estimated coefficients used for the modal control technique are processed by the dynamic compensation matrix D^{nn}. The output X^n is first summed with external reference signals Y^n and then transformed to physical actuator forces by the force-transformation compensation matrix $\left[H_e^{nn}\right]^{-1}$.

For this analysis a type 1 control system has been assumed and the integration for each control channel is lumped in the D^{nn} matrix. This matrix is assumed to be diagonal with an integration in each element and a gain of unity. Since the main purpose of this work is to evaluate the steady-state error as a function of the number and location of actuator and sensor points, all other dynamics have been omitted. When given stability, the control system will go to the same steady-state error. Normally, mirror dynamics will have very little effect since the eigenvalues are so large. For example, a 0.76-meter-diameter spherical mirror with a 4.5212-meter radius of curvature, a 60-to-1 ratio of diameter to thickness, and a 3-point kinematic mount has a lowest eigenvalue of 2.59×10^5 rad/sec^2 which corresponds to a frequency of 81 hertz (ref. 7). The lowest eigenvalue for a 3.05-meter-diameter mirror with the same f-number and diameter-to-

thickness ratio is approximately 1.47×10^4 rad/sec^2 which corresponds to a frequency of 19.3 hertz. (See ref. 7.) Despite the lack of low-order dynamics in the dynamic compensation matrix, the stability of the control loop and interaction between control channels must be evaluated for different actuator and sensor locations, for the design of the $\left[U_e^{NN}\right]^{-1}$ matrix, and later for the design of the $\left[H_e^{NN}\right]^{-1}$ matrix.

The approach for calculating the force-transformation matrices is only summarized in this paper for completeness since it is derived in reference 2. The U^{MM} matrix is partitioned into a (3×3) matrix as

$$\left[U^{MM}\right] = \left[\begin{array}{c|c|c} U^{nn} & U^{nr} & U^{nR} \\ \hline U^{rn} & U^{rr} & U^{rR} \\ \hline U^{Rn} & U^{Rr} & U^{RR} \end{array}\right] \tag{4}$$

where the rows correspond to grid-point locations and the columns represent the modes. Normally, the modes will be in numerical order whereas the grid points will not have any special distribution. The force-transformation matrices are determined from the n points where actuator forces are applied to the mirror and, for the case where the force acts over a very localized area, are obtained (ref. 3) by transposing the first row in equation (4) as

$$H^{nn} = \left[U^{nn}\right]^T \tag{5a}$$

$$H^{rn} = \left[U^{nr}\right]^T \tag{5b}$$

$$H^{Rn} = \left[U^{nR}\right]^T \tag{5c}$$

The eigenvalue matrices are diagonal with all positive coefficients and are derived by again partitioning according to the n, r, and R sets as

$$\left[\Lambda^{MM}\right]^{-1} = \left[\begin{array}{c|c|c} \Lambda^{nn} & 0 & 0 \\ \hline 0 & \Lambda^{rr} & 0 \\ \hline 0 & 0 & \Lambda^{RR} \end{array}\right]^{-1} \tag{6}$$

The figure-error sensor only observes N points on the mirror surface. Perfect alinement and a large signal-to-noise ratio are assumed for this sensor. The output signal W^N is, therefore, a perfect representation of the N measured points on the

mirror. The relationship between the input and output of the figure-error sensor is given as

$$W^N = \left[I^{NN} \quad \vdots \quad 0^{NR} \right] W^M \tag{7}$$

where W^M is partitioned such that the first N coefficients represent the measured points, and 0 represents a null matrix. Substituting equation (2) into (7) yields

$$W^N = \left[I^{NN} \quad \vdots \quad 0^{NR} \right] U^{MM} C^M \tag{8}$$

The displacement transformation matrix can be partitioned into a (2×2) matrix as

$$\left[U^{MM} \right] = \left[\begin{array}{c|c} U^{NN} & U^{NR} \\ \hline U^{RN} & U^{RR} \end{array} \right] \tag{9}$$

where the first N rows correspond to the N observed displacement points on the mirror surface and the first N columns are the sensed modes desired. Substituting equation (9) into (8) and using equations (1) and (3) yields

$$W^N = \left[U^{NN} \quad \vdots \quad U^{NR} \right] \left\{ \begin{array}{c} C^N \\ \hline C^R \end{array} \right\} \tag{10}$$

which relates the figure-sensor output to the modal-displacement vector. The estimated modal-displacement vector is related to the figure-sensor output vector by

$$\hat{C}^N = \left[U_e{}^{NN} \right]^{-1} W^N \tag{11}$$

Substituting equation (10) into (11) gives

$$\hat{C}^N = \left[U_e{}^{NN} \right]^{-1} U^{NN} C^N + \left[U_e{}^{NN} \right]^{-1} U^{NR} C^R \tag{12}$$

with the following relationships defined as

$$\left[U_e{}^{NN} \right]^{-1} \left[U^{NN} \right] = \left[\begin{array}{c|c} V^{nn} & V^{nr} \\ \hline V^{rn} & V^{rr} \end{array} \right] \tag{13a}$$

$$\left[U_e^{NN}\right]^{-1}\left[U^{NR}\right] = \begin{bmatrix} V^{nR} \\ \hline V^{rR} \end{bmatrix} \tag{13b}$$

By substituting equations (13) into (12) and using equation (3), the estimated modal-displacement coefficients become

$$\begin{Bmatrix} \hat{C}^n \\ \hline \hat{C}^r \end{Bmatrix} = \left[\begin{array}{c|c} V^{nn} & V^{nr} \\ \hline V^{rn} & V^{rr} \end{array}\right] \begin{Bmatrix} C^n \\ \hline C^r \end{Bmatrix} + \begin{bmatrix} V^{nR} \\ \hline V^{rR} \end{bmatrix} C^R \tag{14}$$

In the modal control technique, only the first n modes are used for control. Since these n coefficients are inputs to integrators, a differential equation can be written as

$$\dot{X}^n = \hat{C}^n = V^{nn}C^n + V^{nr}C^r + V^{nR}C^R \tag{15}$$

Relating the actuator forces to the input reference signal and to the state variables gives

$$\alpha^n = \left[H_e^{nn}\right]^{-1} Y^n - \left[H_e^{nn}\right]^{-1} X^n \tag{16}$$

The modal-displacement vectors are related to the force vector by

$$C^n = q^n + \left[\Lambda^{nn}\right]^{-1} H^{nn}\alpha^n \tag{17a}$$

$$C^r = q^r + \left[\Lambda^{rr}\right]^{-1} H^{rn}\alpha^n \tag{17b}$$

$$C^R = q^R + \left[\Lambda^{RR}\right]^{-1} H^{Rn}\alpha^n \tag{17c}$$

The modal-displacement vectors can be related to the reference vector and state variable vector by substituting equation (16) into (17) as

$$C^n = q^n + \left[\Lambda^{nn}\right]^{-1} H^{nn}\left[H_e{}^{nn}\right]^{-1} Y^n - \left[\Lambda^{nn}\right]^{-1} H^{nn}\left[H_e{}^{nn}\right]^{-1} X^n \tag{18a}$$

$$C^r = q^r + \left[\Lambda^{rr}\right]^{-1} H^{rn}\left[H_e{}^{nn}\right]^{-1} Y^n - \left[\Lambda^{rr}\right]^{-1} H^{rn}\left[H_e{}^{nn}\right]^{-1} X^n \tag{18b}$$

$$C^R = q^R + \left[\Lambda^{RR}\right]^{-1} H^{Rn}\left[H_e{}^{nn}\right]^{-1} Y^n - \left[\Lambda^{RR}\right]^{-1} H^{Rn}\left[H_e{}^{nn}\right]^{-1} X^n \tag{18c}$$

In all previous work, matrix $\left[H_e{}^{nn}\right]^{-1}$ has always been assumed as the inverse of matrix H^{nn}, allowing terms in equation (18a) to cancel. The state-space first-order differential equation that describes the modal control loop is obtained by substituting equations (18) into (15) and recombining terms. In general form, the equation becomes

$$\dot{X}^n = A^{nn}X^n + B^{nM}q^M + F^{nn}Y^n \tag{19}$$

and equations (18) become, respectively,

$$C^n = E^{nn}X^n + q^n + G^{nn}Y^n \tag{20a}$$

$$C^r = E^{rn}X^n + q^r + G^{rn}Y^n \tag{20b}$$

$$C^R = E^{Rn}X^n + q^R + G^{Rn}Y^n \tag{20c}$$

where

$$A^{nn} = -\left[V^{nn}\Lambda^{nn^{-1}}H^{nn}H_e{}^{nn^{-1}} + V^{nr}\Lambda^{rr^{-1}}H^{rn}H_e{}^{nn^{-1}} + V^{nR}\Lambda^{RR^{-1}}H^{Rn}H_e{}^{nn^{-1}}\right] \tag{21a}$$

$$B^{nM} = \left[V^{nn} \;\vdots\; V^{nr} \;\vdots\; V^{nR}\right] \tag{21b}$$

$$F^{nn} = -A^{nn} \tag{21c}$$

$$E^{nn} = -\left[\Lambda^{nn}\right]^{-1} H^{nn}\left[H_e{}^{nn}\right]^{-1} \tag{21d}$$

$$E^{rn} = -\left[\Lambda^{rr}\right]^{-1} H^{rn}\left[H_e{}^{nn}\right]^{-1} \tag{21e}$$

$$E^{Rn} = -\left[\Lambda^{RR}\right]^{-1} H^{Rn}\left[H_e{}^{nn}\right]^{-1} \tag{21f}$$

$$G^{nn} = -E^{nn} \tag{21g}$$

$$G^{rn} = -E^{rn} \tag{21h}$$

$$G^{Rn} = -E^{Rn} \tag{21i}$$

By using the relationship given in equation (21c), the steady-state solution to equation (19) for a step-input disturbance q is

$$X_{ss}^{n} = -\left[A^{nn}\right]^{-1} B^{nM_q M} + Y^{n} \tag{22}$$

provided the coefficient matrix A^{nn} is nonsingular and all of its eigenvalues are distinct and have negative real parts. The restriction of distinct eigenvalues is a practical consideration to simplify the solution shown in equation (22) and does not limit the general equation (19). For all computer runs, the eigenvalues have always been found to be distinct. Once the state variable vector is calculated, the modal-displacement coefficients can be found by substituting equation (22) into equations (20) and using the relationships in equations (21) as

$$C^{n} = q^{n} - E^{nn}\left[A^{nn}\right]^{-1} B^{nM_q M} \tag{23a}$$

$$C^r = q^r - E^{rn}\left[A^{nn}\right]^{-1} B^{nM} q^M \tag{23b}$$

$$C^R = q^R - E^{Rn}\left[A^{nn}\right]^{-1} B^{nM} q^M \tag{23c}$$

The performance index used for all analysis in this paper is defined as the rms error of the mirror surface. The derivation is given in reference 3 and shows that the performance index J can be represented in terms of the modal-displacement coefficients as

$$J = \sqrt{\left[C^M\right]^T C^M} \tag{24}$$

where the C^M vector is taken from the solution of equations (23).

DEVELOPMENT OF OPTIMAL CONTROLLER

In reference 3 an optimal control law was defined as the least squares fit to the desired shape. An open-loop optimal control law was derived where actuator forces were found that minimize the square of the performance index in equation (24). In this paper, a slightly different approach is used where an optimal controller is developed for use in a closed-loop control system. The state-space differential equations that describe the control loop with this controller are shown at the end of this section after the controller is developed.

It is first assumed that a perfect figure-error sensor is used and that all M points on the mirror surface are observed ($R = 0$). After the controller is developed, it will be combined with the other components in the control loop and equations will be developed for the case with unobserved mirror displacements. The change in performance index with respect to the actuator forces is derived in reference 3 as

$$\frac{\partial J^2}{\partial \alpha^n} = 2\left\{\left[\Lambda^{MM}\right]^{-1} H^{Mn}\right\}^T \left\{\left[\Lambda^{MM}\right]^{-1} H^{Mn}\right\} \alpha^n + 2\left\{\left[\Lambda^{MM}\right]^{-1} H^{Mn}\right\}^T q^M \tag{25}$$

where H^{Mn} and Λ^{MM} are defined in equations (5a), (5b), and (6). For a perfect figure-error sensor with 100-percent observability of the mirror surface, the estimated modal-displacement vector $\hat{C}^M$ is equivalent to the actual modal-displacement vector C^M. Solving for q^M in equations (17a) and (17b), making use of equation (1), and substituting into equation (25) yields

$$\frac{\partial J^2}{\partial \alpha^n} = 2\left\{\left[\Lambda^{MM}\right]^{-1} H^{Mn}\right\}^T \hat{C}^M = 0 \tag{26}$$

where the equation is set equal to zero since the minimum value is desired. Computer results show (see last section of the paper) that the minimum value is always obtained for the perfect figure-error sensor case since the error is always less than that for the modal control law. Partitioning equation (26) into the n and r sets ($R = 0$) and defining the vector as $\dot{X}^n$ yields

$$\dot{X}^n = U^{nn}\left[\Lambda^{nn}\right]^{-1} \hat{C}^n + U^{nr}\left[\Lambda^{rr}\right]^{-1} \hat{C}^r = 0 \tag{27}$$

Equation (27) is the basic equation for the optimal controller and shows that all of the estimated modal-displacement coefficients are used and weighted by their eigenvalues and corresponding eigenvectors. Since the control law states that vector $\dot{X}^n$ must be forced to zero, each of the n signals is an input to an integrator. Figure 4 is a block diagram of the least-squares optimal controller and shows vector $\dot{X}^n$ as the input to the dynamic compensation matrix. In a practical situation there will always be modes that are neither observed nor controlled ($R \neq 0$). For this case, the assumption that $\hat{C}^M$ and C^M are equal is not completely true. The effect of this assumption is shown in the computer results discussed later in this paper.

The control-system equations with the optimal controller are essentially the same as those described for the modal control technique. By letting matrix $\left[H_e{}^{nn}\right]^{-1}$ be an identity matrix to mechanize equation (27), equations (7) to (18), with the exception of equation (15), are applicable to both control loops. Another reason for letting $\left[H_e{}^{nn}\right]^{-1}$ be an identity matrix is described in appendix A, section II. Equation (15) is replaced by

$$\dot{X}^n = U^{nn}\left[\Lambda^{nn}\right]^{-1}\hat{C}^n + U^{nr}\left[\Lambda^{rr}\right]^{-1}\hat{C}^r \tag{28}$$

and equation (14) remains the same as

$$\hat{C}^n = V^{nn}C^n + V^{nr}C^r + V^{nR}C^R \tag{29}$$

and

$$\hat{C}^r = V^{rn}C^n + V^{rr}C^r + V^{rR}C^R \tag{30}$$

with V^{nn}, V^{nr}, V^{nR}, V^{rn}, V^{rr}, and V^{rR} defined in equations (13).

The general form for the state-space differential equation is similar to that for the modal control loop (eq. (19)) and is

$$\dot{X}^n = S^{nn}X^n + Z^{nM}q^M + L^{nn}Y^n \tag{31}$$

where

$$\begin{aligned} S^{nn} = -\Big[&\left(U^{nn}\Lambda^{nn^{-1}}V^{nn} + U^{nr}\Lambda^{rr^{-1}}V^{rn}\right)\Lambda^{nn^{-1}}H^{nn} \\ &+ \left(U^{nn}\Lambda^{nn^{-1}}V^{nr} + U^{nr}\Lambda^{rr^{-1}}V^{rr}\right)\Lambda^{rr^{-1}}H^{rn} \\ &+ \left(U^{nn}\Lambda^{nn^{-1}}V^{nR} + U^{nr}\Lambda^{rr^{-1}}V^{rR}\right)\Lambda^{RR^{-1}}H^{Rn}\Big] \end{aligned} \tag{32a}$$

$$Z^{nM} = \left[\left(U^{nn}\Lambda^{nn^{-1}}V^{nn} + U^{nr}\Lambda^{rr^{-1}}V^{rn}\right)\middle|\left(U^{nn}\Lambda^{nn^{-1}}V^{nr} + U^{nr}\Lambda^{rr^{-1}}V^{rr}\right)\middle|\left(U^{nn}\Lambda^{nn^{-1}}V^{nR} + U^{nr}\Lambda^{rr^{-1}}V^{rR}\right)\right] \tag{32b}$$

$$L^{nn} = -S^{nn} \tag{32c}$$

Equations (29) to (32) show how the optimal controller, which was derived for the case with $R = 0$, is used in a control system where all physical displacements on the mirror are not observed ($R \neq 0$). The effect of using the optimal controller in a system with unobserved mirror displacements is shown in the last sections of this paper. Equations (20) for the modal-displacement coefficients, with the relationships in equations (21d) to (21i) and with the force-transformation compensation matrix $\left[H_e^{nn}\right]^{-1}$ an identity, are applicable to the optimal control loop. Replacing coefficient matrices A^{nn} and B^{nM} by S^{nn} and Z^{nM}, respectively, in equations (22) and (23) results in the steady-state solutions to a step-input disturbance q^M for the state variables X_{ss}^n and the model-displacement coefficients. Both control laws have similar stability requirements that are described in the next section.

STABILITY, CONTROLLABILITY, AND OBSERVABILITY

Although the only dynamics considered in the control loop is an integration in each controlled channel, the effect of matrices $\left[U_e^{NN}\right]^{-1}$ and $\left[H_e^{nn}\right]^{-1}$ on system stability must be evaluated. Improper selection of these matrices can result in interaction between control channels resulting in complex conjugate eigenvalues and/or positive roots. Complex conjugate roots have been obtained for certain selections of the mode-analyzer matrix, and positive roots have been obtained for an improper selection of the force-transformation compensation matrix. For a multichannel control system with only one integration in each control channel, complex conjugate roots indicate a coupling between control channels.

The subsequent analysis is made by using the symbols defined for the modal control system. However, the analysis is also valid for the optimal control system if S^{nn} (eq. (32a)) is used in place of A^{nn} (eq. (21a)) and L^{nn} (eq. (32c)) is used in place of F^{nn} (eq. (21c)). Since the control system analyzed in this paper is linear and time-invariant, asymptotic stability can be determined from the coefficient matrix A^{nn} in equation (19). (See ref. 8.) If the eigenvalues of this matrix have all negative real parts, then the control system is stable. As an additional criterion for the solution vector in equation (22) to be valid, all eigenvalues of matrix A^{nn} must be distinct. From the many computer runs that have been made, the eigenvalues of this matrix have always been distinct, although complex conjugate pairs have been found.

The definitions for controllability and observability are given in reference 8 and, therefore, only the basic equations for the control system defined by equations (19)

and (20) are presented in this paper. This control system is completely state controllable if and only if the composite $(n \times n^2)$ matrix P_{sc} is of rank n where

$$P_{sc} = \left[F^{nn} \;\vdots\; A^{nn}F^{nn} \;\vdots\; --- \;\vdots\; \left[A^{nn}\right]^{(n-1)} F^{nn} \right] \tag{33}$$

By using the relationship in equation (21c), equation (33) becomes

$$P_{sc} = -\left[A^{nn} \;\vdots\; \left[A^{nn}\right]^{2} \;\vdots\; --- \;\vdots\; \left[A^{nn}\right]^{n} \right] \tag{34}$$

and must be of rank n for complete state controllability.

The system described by equations (19) and (20) is completely output controllable if and only if the composite $\left[n \times n(n+1)\right]$ matrix P_{oc} is of rank n where

$$P_{oc} = \left[E^{nn}F^{nn} \;\vdots\; E^{nn}A^{nn}F^{nn} \;\vdots\; --- \;\vdots\; E^{nn}\left[A^{nn}\right]^{(n-1)} F^{nn} \;\vdots\; G^{nn} \right] \tag{35}$$

By using the relationships in equations (21c) and (21g), equation (35) becomes

$$P_{oc} = -\left[E^{nn}A^{nn} \;\vdots\; E^{nn}\left[A^{nn}\right]^{2} \;\vdots\; --- \;\vdots\; E^{nn}\left[A^{nn}\right]^{n} \;\vdots\; E^{nn} \right] \tag{36}$$

and must be of rank n for complete output controllability. Notice that only the modal-displacement coefficients defined by equations (20) have been considered since, with n actuators, only n channels can be controlled.

Equations (19), (20a), and (20b) are used to check for observability. Modal channel C^n is completely observable if and only if the composite $(n \times n^2)$ matrix P_{obn} is of rank n where

$$P_{obn} = \left[\left(E^{nn}\right)^{*} \;\vdots\; \left(A^{nn}\right)^{*}\left(E^{nn}\right)^{*} \;\vdots\; --- \;\vdots\; \left(A^{nn}\right)^{*(n-1)}\left(E^{nn}\right)^{*} \right] \tag{37}$$

The symbol * represents the conjugate transpose of the corresponding matrix in parentheses. Modal channel C^r is completely observable if and only if the composite $(n \times nr)$ matrix P_{obr} is of rank n where

$$P_{obr} = \left[\left(E^{rn}\right)^* \;\vdots\; \left(A^{nn}\right)^* \left(E^{rn}\right)^* \;\vdots\; --- \;\vdots\; \left(A^{nn}\right)^* \left(E^{rn}\right)^* \right] \tag{38}$$

Both stability and controllability were checked in all computer runs. For all cases, the first partition in equations (34) and (36) was found to be sufficient.

SELECTION OF ACTUATOR AND SENSOR LOCATIONS

Two of the most important steps for obtaining good results in controlling the figure of a large primary mirror are the selection of actuator locations and figure-error sensor locations. The approach used here is to select actuator locations on the basis of minimizing that part of the potential energy which is in the uncontrolled modes, whereas figure-error sensor locations are selected to minimize the potential energy of the unobserved modes. For the remainder of this discussion the approach will be described in terms of actuator locations since the criteria for actuator and sensor locations are identical.

It is first assumed that M external loads representing actuator forces α^M are exerted on the mirror causing W^M finite mirror displacements. A technique and justification for selecting n of the M actuator locations will then be described. Finally, specific locations will be shown for 4, 7, 10, 15, and 20 actuator cases.

The potential energy I_p is related to the flexibility matrix T^{MM} and actuator forces as

$$I_p = \frac{1}{2}\left[\alpha^M\right]^T T^{MM} \alpha^M \tag{39}$$

By using the relationship between the eigenvalue matrix Λ^{MM} and the stiffness matrix K^{MM} (see ref. 9) as

$$\Lambda^{MM} = \left[U^{MM}\right]^T K^{MM} U^{MM} \tag{40}$$

where the eigenvectors are normalized such that

$$\left[U^{MM}\right]^T M_m{}^{MM} U^{MM} = I^{MM} \tag{41}$$

and where M_m is the mass matrix, and by noting that the flexibility matrix is the inverse of the stiffness matrix, the equation for potential energy becomes

$$I_p = \frac{1}{2}\left[\alpha^M\right]^T \left\{U^{MM}\left[\Lambda^{MM}\right]^{-1}\left[U^{MM}\right]^T\right\}\alpha^M \tag{42}$$

The flexibility matrix is the term inside the braces in equation (42) and is shown in terms of the eigenvectors and eigenvalues of the mirror. Partitioning the flexibility matrix into two parts corresponding to n controlled modes and p uncontrolled modes where

$$p = r + R \tag{43}$$

yields

$$U^{MM}\left[\Lambda^{MM}\right]^{-1}\left[U^{MM}\right]^T = \left[U^{Mn} \;\vdots\; U^{Mp}\right]\left[\begin{array}{c|c} \Lambda^{nn} & 0 \\ \hline 0 & \Lambda^{pp} \end{array}\right]^{-1}\left[\begin{array}{c} \left[U^{Mn}\right]^T \\ \hline \left[U^{Mp}\right]^T \end{array}\right] \tag{44}$$

Substituting equation (44) into equation (42) gives

$$I_p = \frac{1}{2}\left[\alpha^M\right]^T \left\{U^{Mn}\left[\Lambda^{nn}\right]^{-1}\left[U^{Mn}\right]^T\right\}\alpha^M + \frac{1}{2}\left[\alpha^M\right]^T \left\{U^{Mp}\left[\Lambda^{pp}\right]^{-1}\left[U^{Mp}\right]^T\right\}\alpha^M \tag{45}$$

where the potential energy is a function of the energy in the controlled and uncontrolled modes of free vibration. That part of the potential energy I_{pu} that is in the uncon-

trolled modes, described by the second term in equation (45), can be partitioned according to the n selected actuator locations into

$$I_{pu} = \frac{1}{2}\begin{bmatrix} \alpha^n \\ \hline \alpha^p \end{bmatrix}^T \left[\begin{array}{c|c} T^{nn} & T^{np} \\ \hline T^{pn} & T^{pp} \end{array}\right] \begin{bmatrix} \alpha^n \\ \hline \alpha^p \end{bmatrix} \tag{46}$$

and since α^p is zero, equation (46) reduces to

$$I_{pu} = \frac{1}{2}\left[\alpha^n\right]^T T^{nn}\alpha^n \tag{47}$$

Equation (47) shows the work done on the uncontrolled modes as a function of the actuator locations and forces, but it does not indicate how these locations are selected. The main idea is to select actuator locations that give a minimum value for I_{pu}. One approach is to try all possible combinations of actuators. The problem with this approach is that the number of possible combinations becomes unwieldy. For example, if 7 actuators are used to control 7 modes ($n = 7$) and 250 possible locations are available ($p = 243$), the number of possible combinations is 1.13×10^{13}.

An alternate and less time-consuming procedure that is used in this paper is to work with the flexibility matrix of the uncontrolled modes. (See eq. (46).) The M diagonal elements of this matrix are extracted and plotted on a contour map at the corresponding grid-point coordinates. Minimum values on these contour maps, except near support points which are always low, are selected for actuator locations. These diagonal coefficients and their corresponding off-diagonal coefficients form the matrix T^{nn} (eq. (47)). Since the flexibility matrix is symmetric and positive definite, the approach assumes that if all diagonal elements of T^{nn} are small and approximately the same value, then the off-diagonal coefficients will also be small and probably smaller than the diagonal coefficients.

The validity of this assumption and the physical significance is described as follows: The coefficients of T^{nn} are described by

$$\sum_{j=n+1}^{M} \lambda_j^{-1} u_{ij} u_{kj} \qquad \begin{array}{l} (i = k \text{ for diagonal coefficients;} \\ \quad i \neq k \text{ for off-diagonal coefficients)} \end{array} \tag{48}$$

where u represents a coefficient of matrix U^{Mp}, i and k represent the row and column indices of T^{nn}, respectively, and λ is an eigenvalue of matrix Λ^{pp}. For any

diagonal element in T^{nn}, each term in equation (48) is positive and the summation represents a maximum. The off-diagonal terms can be positive or negative and the summation will probably be less than the corresponding diagonal coefficients since the same terms are included in both summations. When considering only the diagonal terms, equation (48) shows that each element belonging to an eigenvector is squared, weighted by its eigenvalue, and then summed over all the uncontrolled modes. Selection of the smallest values for actuator locations is motivated by a philosophy similar to selecting a common node line for all the uncontrolled modes. Although the actuators will not be on the mode lines of any particular mode, they will probably be near the node lines of the most predominant uncontrolled modes.

Figure 5 represents contour maps obtained by taking the diagonal elements of the flexibility matrix for the uncontrolled modes for 4, 7, 10, 15, and 20 actuators cases, respectively. The peak value on each map is normalized to 100 percent, and the crosses indicate the locations of actuators (or sensors). These actuator locations have been used in the computer runs described later in this paper. The four actuator locations shown in figure 5(a) are identical to one of the best cases found from a complete search of 58 possible grid points using uncorrelated errors (ref. 3). The seven locations in figure 5(b) are among the several best cases shown in reference 3, although all seven are not shown simultaneously. The best seven in the reference were not selected from a complete search of all the grid points. The contour maps are used to find approximate locations for actuators. Once the general area is decided upon, a computer printout is referenced to find the exact location of the minimum.

The technique of selecting actuator locations at points where the potential energy of the uncontrolled modes is small completely ignores the controlled modes. There are occasions when matrices H^{nn} (see eq. (5a)) and U^{NN} (see eq. (9)) become singular or ill-conditioned causing extremely poor results. For these cases, the relocation of one actuator or sensor has eliminated this problem. Physically, an ill-conditioned or singular matrix means that at least one controlled mode, considering only actuator locations, is essentially a linear combination of the other controlled modes. The modes can be controlled in the ill-conditioned case, but only with very large actuator forces causing increased excitation of the higher order modes. A specific example of an ill-conditioned case is described in the last section of this paper.

DESIGNING THE MODE ANALYZER

The mode-analyzer matrix $\left[U_e{}^{NN}\right]^{-1}$ in the controller section (figs. 3 and 4) of the control loop transforms the N measured displacements on the mirror surface from

physical to modal coordinates. The accuracy of the estimated modal-displacement vector $\hat{C}^N$ is a function of the method used to design this matrix.

One method of choosing the mode analyzer is to invert matrix U^{NN} defined in equation (9). (See ref. 2.) By doing this, equation (13a) becomes an identity matrix, and for $N > n$ the coefficient matrices A^{nn} and S^{nn} for the modal and optimal control laws (see eqs. (21a) and (32a)) become, respectively,

$$A^{nn} = -\left[\Lambda^{nn}\right]^{-1} \tag{49}$$

and

$$S^{nn} = \left[U^{nn}\Lambda^{nn-2}H^{nn} + U^{nr}\Lambda^{rr-2}H^{rn}\right] \tag{50}$$

The derivation of equations (49) and (50) is given in appendix A, section I and assumes that the modes that are neither controlled nor observed are negligible. This is a realistic assumption since enough figure-sensor points will probably be used to get a good estimate of the modal-displacement coefficients. Both of the aforementioned coefficient matrices always have negative eigenvalues indicating that the closed-loop control system is always stable.

A second approach for choosing the mode analyzer is first to invert the displacement transformation matrix U^{MM} in equation (9) and then to partition the N rows and columns corresponding to the N sensed modes and grid points, respectively (ref. 4). For this approach the coefficient matrices A^{nn} and S^{nn} become

$$A^{nn} = -\left[V^{nn}\Lambda^{nn-1} + V^{nr}\Lambda^{rr-1}H^{rn}H^{nn-1}\right] \tag{51}$$

where

$$\left[H_e{}^{nn}\right]^{-1} = \left[H^{nn}\right]^{-1}$$

and

$$S^{nn} = -\left[\left(U^{nn}\Lambda^{nn^{-1}}V^{nn} + U^{nr}\Lambda^{rr^{-1}}V^{rn}\right)\Lambda^{nn^{-1}}H^{nn}\right.$$

$$\left. + \left(U^{nn}\Lambda^{nn^{-1}}V^{nr} + U^{nr}\Lambda^{rr^{-1}}V^{rr}\right)\Lambda^{rr^{-1}}H^{rn}\right] \tag{52}$$

where $\left[H_e{}^{nn}\right]^{-1}$ is an identity matrix. Again it is assumed that the modes that are neither controlled nor observed are negligible and $N > n$. Neither equation (51) nor (52) has any special properties for stability. Matrix A^{nn}, which was uncoupled for $R = 0$ in equation (49), is now a full matrix with interaction between various control channels. Matrix S^{nn}, which had positive definite and symmetric properties in equation (50), has neither of these properties in equation (52). Results from computer runs show that complex conjugate eigenvalues can result when using the second approach for designing the mode analyzer.

The two techniques for designing the mode analyzer have been evaluated by computer runs for both the modal and optimal control laws. The four possible cases are defined as follows:

Modal control law

Method 1: $$\left[U_e{}^{NN}\right]^{-1} U^{NN} = I \tag{53a}$$

Method 2: $$\left[U_e{}^{NN}\right]^{-1} U^{NN} \neq I \tag{53b}$$

Optimal control law

Method 3: $$\left[U_e{}^{NN}\right]^{-1} U^{NN} = I \tag{53c}$$

Method 4: $$\left[U_e{}^{NN}\right]^{-1} U^{NN} \neq I \tag{53d}$$

In the next section the results from several computer runs using methods 1 to 4 for three different initial error distributions are discussed.

CONTROL-SYSTEM COMPUTER RESULTS

The goal of this section is to tie together all of the previously described theory and compare it to the computer results for the various designs. The results show the steady-state error remaining for various numbers and locations of actuators and figure-error sensors. These runs are made for each of the two control laws and for the two mode-analyzer designs. Included in this section is a description of three error distributions used to get a good variation of results.

All computer runs in this paper have been made for a solid, spherical mirror (without a central hole) with a diameter of 0.762 meter, a diameter-to-thickness ratio of 60 to 1, a radius of curvature of 4.5212 meters, and a 3-point kinematic mount located 120° apart. The finite-element structural model of this mirror is shown in figure 2 and consists of 462 triangular elements and 253 grid points. The supports are located at grid points 15, 119, and 247 as described earlier in this paper. A modal analysis of this mirror has been made by using the NASTRAN structural analysis program (ref. 6) which computed the eigenvalues and eigenvectors needed for the control-system analysis. Fifty-eight modes have been used for the control-system simulation since this should provide sufficient accuracy for the final analysis. A more complete description of the mirror dynamics can be found in reference 7 which includes the natural frequencies of vibration and contour maps for the first 10 mode shapes. Figure 6 contains a plot of the first 58 eigenvalues for the mirror used in this analysis.

Three different error distributions have been used to get a reasonably good distribution of results. Since actuator and sensor locations are selected independent of the initial error, the final results should be reasonably good for all three error distributions. Figure 7 contains contour maps, normalized to a maximum of -100, representing the three different initial errors. Figure 7(a) shows error distribution number 1 and represents the fabrication error measured from an actual mirror described in reference 5 with the physical properties described earlier in this section and with an rms figure error of one-half wavelength (approximately 0.3 μm). Figure 7(b) shows error distribution number 2 and was arbitrarily generated by making the initial modal disturbance vector q^M decrease very rapidly with mode number. The contour plot for this error is very similar to that for mode 1 of the mirror. Error distribution number 3 (fig. 7(c)) represents the measured mirror displacement resulting from a thermal disturbance modeled in reference 4 on an actual mirror which has the same properties as the mirror described in this paper.

The initial-error disturbance vector in modal coordinates is calculated from the physical displacement vector by

$$q^M = \left[U^{MM}\right]^{-1} W^M \tag{54}$$

These modal-displacement coefficients are used to determine the number of actuators required to reduce the initial error by a predetermined amount, assuming uncorrelated errors (ref. 3). The rms error Q remaining after n modes are deleted is calculated by

$$Q = \left[\sum_{i=n+1}^{M} q_i^2\right]^{1/2} \tag{55}$$

The percent of rms error left after deleting the n controlled mode is shown in figure 8 for the three error distributions. For very good actuator and figure-error sensor locations, the error left should follow these initial-error curves.

Typical computer runs made for each error distribution include varying the number of actuators and sensors in different combinations. Methods 1 to 4 relating different combinations of control laws and mode analyzers and defined in a previous section entitled "Designing the Mode Analyzer" are checked for each run. These methods will be designated by a number next to the corresponding data point in all of the following figures. Actuator and sensor locations for the various cases are shown by crosses in figure 5. The corresponding grid-point numbers for these cases are listed in table I and refer to the finite-element model in figure 2. The actuator locations are based upon the vectors q_i being uncorrelated, and a deterministic error is used only to evaluate the results.

All of the computer results shown in this paper are plotted as a percent of rms error left for a specific number of actuators and sensors. In figure 9 this rms error is plotted as a function of the number of actuators with a perfect figure-error sensor that observed all points on the mirror surface and for initial error distribution number 1. The predicted error (eq. (55)) is plotted as a reference to show the desired goal for each number of actuators. For the case where all points on the mirror surface are observed by the figure-error sensor, the optimal control law (methods 3 and 4) is always equal to or superior to the modal control law (methods 1 and 2). The difference between the predicted error curve and the calculated data points indicates the amount of error generated

TABLE I.- GRID POINTS FOR 4, 7, 10, 15, AND 20 ACTUATOR AND SENSOR CASES

Number	Actuator and sensor locations for cases –				
	4	7	10	15	20
1	31	21	21	11	12
2	127	57	57	18	18
3	133	83	79	56	47
4	217	127	83	60	50
5		182	110	64	53
6		187	124	68	71
7		232	178	124	74
8			182	127	88
9			187	131	111
10			232	134	122
11				186	126
12				190	134
13				198	164
14				229	170
15				243	173
16					206
17					209
18					212
19					229
20					244

in the higher order modes. For the 4- and 7-actuator cases, the error generated by the control system subtracts from the initial error (see eqs. (23)); whereas for the 15- and 20-actuator cases, the error generated by the control system adds to the initial error in the higher order modes. Since the actuator locations are selected to minimize the potential energy in the uncontrolled modes and are not at node lines, it is highly improbable that locations can be selected that are completely independent of the uncontrolled modes. The best that can be done is to use several error distributions and select actuator locations that minimize the differences for all cases.

The effect on the steady-state accuracy of decreasing the number of sensor points for 4 and 7 actuators is shown in figures 10 and 11, respectively. The predicted error level (from fig. 9) is 67.3 percent for the 4-actuator case and 47.1 percent for the

7-actuator case. Notice that for the case of an equal number of actuators and sensors, all four methods give the same results. (See appendix A, section II.) When there are a few more sensors than actuators, the error increases and is probably the result of poor estimates for the modal-displacement coefficients. In both figures 10 and 11, 15 sensor points give results that are almost as good as the results from 58 sensor points; this is defined as the case with all points on the mirror surface observed. In general, method 3 again gives the best results, although this is not always true for a nonperfect figure-error sensor.

In order to demonstrate that poor actuator locations can cause poor results, the actuator located at grid point 127 (7-actuator case) was changed to grid point 132. The relative amplitude on the contour map in figure 5(b) is 1.8 percent higher at grid point 132 Figure 12 shows a plot for the 7-actuator case with several different sensor points and locations. For 10 sensor points, the final error for method 2 is 102 percent and for method 4 it is 99 percent.

Another good example is shown by the 20-actuator and 20-sensor cases. For these cases, grid point 98 rather than grid point 88 would normally be selected from the contour map in figure 5(e) (table I). The results for these cases using the three error distributions are shown in table II. For the cases with 20 actuators and 58 sensors, the results for methods 1 and 2 are extremely poor; whereas the results for methods 1 and 3 are extremely poor for the cases with 7 actuators and 20 sensors. Matrix H^{nn} in equation (5a) for the 20-actuator cases is the transpose of matrix U^{NN} in equation (9) for the 20-sensor cases. These matrices appear to be ill-conditioned as demonstrated by the norm which is -2.12×10^{-4}. (See ref. 10.) In comparison, the norm of these matrices when grid point 88 is substituted for grid point 98 is -1.23×10^{-2}. Although the results using grid point 88 are reasonably good, it is likely that better results could be obtained by trying other locations for this actuator or sensor, since grid point 88 is next to grid point 71. In general, a change of 1 actuator or 1 sensor will not cause results as poor as those shown in this example.

TABLE II.- STEADY-STATE ERROR FOR 20-ACTUATOR AND 20-SENSOR CASES USING GRID POINT 98

Error distribution	Cases		Error, percent, for method –			
	Actuators	Sensors	1	2	3	4
1	20	58	383	162	19.1	19.7
1	4	20	66.8	66.0	66.9	65.8
1	7	20	2969	45.9	2945	44.8
2	20	58	57.0	330	0.695	0.702
2	4	20	2.49	1.99	2.41	1.99
3	20	58	487	1089	3.99	3.97
3	4	20	39.0	38.2	38.7	38.2
3	7	20	1438	35.7	1589	35.4

The next set of data to be discussed is for error distribution number 2. Figure 13 shows the rms error left as a function of the number of actuators for the case with all points on the mirror surface observed. Again, the data points are reasonably close to the predicted error curve for the corresponding number of actuators. The effect of changing the number of sensor points for a case with 4 actuators is shown in figure 14. For this error distribution, the results with 7 sensor points is almost as good as the results with 58 sensor points.

Figures 15, 16, and 17 contain the results using error distribution number 3. Again the calculated data in figure 15 follow the predicted error curve closely except for the 20-actuator case. The data points for methods 3 and 4 are still only 5 percent above the initial curve, whereas those for methods 1 and 2 are 10 percent above the curve. These results compare to 3 percent and 8 percent, respectively, for error distribution number 1 (fig. 9). The reason for this small difference from the predicted error curve has been presented previously in this section. Figures 16 and 17 are for the 4- and 7-actuator cases, respectively. For both cases, 15 sensor points appear to be sufficient for good results.

CONCLUDING REMARKS

This paper contains the development of a generalized representation of a controller and then evaluates both a modal control law and an optimal control law that are applicable to figure-error control of a primary error suitable for large orbiting astronomical telescopes. Both computer results and analysis of the equations show that for a perfect figure-error sensor that observes most of the mirror surface, the optimal control law always has a smaller steady-state error than the pure modal control technique, as expected. Analysis also shows that the "optimal" control approach is generally superior for relatively few figure-error sensor locations and for different combinations of actuators and sensors even though the modal-displacement coefficients are not completely known. For decoupling the modal control loop, the force-transformation compensation matrix is chosen as the inverse of the force-transformation matrix associated with the controlled modes. When the optimal control law is applied, the force-transformation compensation matrix is chosen as an identity matrix in order to implement the control law. For either case, the selection of this matrix has no effect on the final steady-state error provided the system is stable. When the number of sensors equals the number of actuators, identical results are obtained from both control laws.

Two techniques for designing the mode analyzer have been presented. One technique is to invert the eigenvector matrix U^{NN} consisting of the N observed mirror locations and the N sensed modes. A second technique is first to invert the displacement transformation matrix U^{MM}, and then to partition the rows and columns corre-

sponding to the N sensed modes and N observed grid points, respectively. Computer results show that, in general, the former technique is superior. The latter technique can cause interaction between controlled channels resulting in complex conjugate roots and possibly an unstable control system.

The technique for selecting actuator and figure-error sensor locations is based upon minimizing that part of the potential energy which is in the uncontrolled and unobserved modes, respectively. An approximate technique for selecting these minimum energy points is based upon plotting the diagonal coefficients of the flexibility matrix of the uncontrolled or unobserved modes on contour maps and then selecting the minimum values. Results from computer analysis show that this technique works quite well and greatly reduces the number of computer searches required to find good locations. All runs are for a solid spherical mirror (without a central hole) with a diameter of 0.762 meter, a diameter-to-thickness ratio of 60 to 1, a radius of curvature of 4.5213 meters, and a 3-point kinematic mount. For each of the three types of initial error used, the rms error left for various numbers of actuators and 58 sensor locations is reasonably close to the predicted value, if assuming uncorrelated errors. For a constant number of actuators (4 or 7) the final error with 15 sensors is almost as good as it is with 58 sensors.

Langley Research Center,
National Aeronautics and Space Administration,
Hampton, Va., June 12, 1973.

APPENDIX A

SPECIAL PROPERTIES OF CONTROL LAWS

I. Stability

Under certain conditions, both the modal and optimal laws have the special property of always having a stable control system. The derivations below are for the control system described in the paper with the dynamic compensation matrix D^{nn} a pure integration.

Modal control law.- This derivation shows that when all physical points on the mirror are observed (R = 0) and the mode-analyzer matrix $\left[U_e^{NN}\right]^{-1}$ and the force-transformation compensation matrix $\left[H_e^{nn}\right]^{-1}$ are chosen as inverse matrices of U^{NN} and H^{nn}, respectively, the type 1 control system in figure 3 is always stable. For these cases, equation (13a) becomes an identity matrix with

$$V^{nn} = I^{nn} \tag{A1a}$$

$$V^{rr} = I^{rr} \tag{A1b}$$

$$V^{rn} = 0 \tag{A1c}$$

$$V^{nr} = 0 \tag{A1d}$$

and equation (13b) is nonexistent. The coefficient matrix A^{nn} in equation (21a) becomes

$$A^{nn} = -\left[\Lambda^{nn}\right]^{-1} \tag{A2}$$

which shows that the eigenvalues associated with the controlled natural modes of vibration of the mirror are also the eigenvalues of the control system. Since the eigenvalue matrix is diagonal with all positive coefficients, all eigenvalues of matrix A^{nn} are negative and real, resulting in a stable control system.

Optimal control law.- This derivation shows that when the mirror surface is completely observable (R = 0) and matrix $\left[U_e^{NN}\right]^{-1}$ is selected as the inverse of matrix U^{NN}, the type 1 control system in figure 3 with the controller in figure 4 is always stable. For these cases, equation (13a) becomes an identity matrix as shown in equations (A1) and equation (13b) is nonexistent. The coefficient matrix S^{nn} in equation (32a) becomes

$$S^{nn} = -\left[U^{nn}\Lambda^{nn^{-2}}H^{nn} + U^{nr}\Lambda^{rr^{-2}}H^{rn}\right] \tag{A3}$$

Using the relationships in equations (5a) and (5b) gives

$$S^{nn} = -\left[U^{nn}\Lambda^{nn^{-2}}U^{nn^T} + U^{nr}\Lambda^{rr^{-2}}U^{nr^T}\right] \tag{A4}$$

The two submatrices inside the brackets in equation (A4) are always real, symmetric, and positive definite, and, therefore, the eigenvalues of matrix S^{nn} are always negative, if assuming a stable control loop.

II. Selection of the Force-Transformation Compensation Matrix

Modal control law.- This derivation shows that the force-transformation compensation matrix $\left[H_e^{nn}\right]^{-1}$ does not affect the final steady-state position in a type 1 control system but does affect the dynamic properties. The coefficient matrix in equation (21a) can be expressed as

$$A^{nn} = -\left[V^{nn}\Lambda^{nn^{-1}}H^{nn} + V^{nr}\Lambda^{rr^{-1}}H^{rn} + V^{nR}\Lambda^{RR^{-1}}H^{Rn}\right]\left[H_e^{nn}\right]^{-1} \tag{A5}$$

and the inverse of equation (A5) is

$$\left[A^{nn}\right]^{-1} = -H_e^{nn}\left[V^{nn}\Lambda^{nn^{-1}}H^{nn} + V^{nr}\Lambda^{rr^{-1}}H^{rn} + V^{nR}\Lambda^{RR^{-1}}H^{Rn}\right] \tag{A6}$$

provided H_e^{nn} and the matrix inside the brackets in equation (A5) are nonsingular. Substituting equations (A6) and (21b) into equation (22) and then solving for the steady-state actuator force α_{ss} in equation (16) yields

$$\alpha_{ss}^{n} = \left[V^{nn}\Lambda^{nn^{-1}}H^{nn} + V^{nr}\Lambda^{rr^{-1}}H^{rn} + V^{nR}\Lambda^{RR^{-1}}H^{Rn}\right]^{-1}\left[V^{nn} \;\vdots\; V^{nr} \;\vdots\; V^{nR}\right]\begin{Bmatrix} q^{n} \\ \hdashline q^{r} \\ \hdashline q^{R} \end{Bmatrix} \tag{A7}$$

Since the steady-state expression for actuator forces does not contain matrix $\left[H_e^{nn}\right]^{-1}$, then the steady-state solution for the modal-displacement coefficients is unaffected by this matrix. (For reference, see eqs. (17).)

<u>Optimal control law</u>.- In the main text, matrix $\left[H_e^{nn}\right]^{-1}$ is considered an identity matrix. If this matrix is not an identity, the coefficient matrix S^{nn} in equation (A3) has a form similar to matrix A^{nn} in equation (A5) as

$$S^{nn} = -\left[U^{nn}\Lambda^{nn^{-2}}H^{nn} + U^{nr}\Lambda^{rr^{-2}}H^{rn}\right]\left[H_e^{nn}\right]^{-1} \tag{A8}$$

The inclusion of matrix $\left[H_e^{nn}\right]^{-1}$ destroys the special properties of a real, symmetric, positive definite matrix for S^{nn}. (See appendix A, section I.)

III. Equal Number of Actuators and Sensors

This section shows that when the number of actuators and sensors are equal, identical results are obtained from both the modal and optimal control laws for a type 1 control system. Further, it has been shown that the modal control law reduces to point control at the actuator locations, and both experimental results and computer simulations have verified these results. For this case, r becomes zero and equations (1) and (3) reduce, respectively, to

$$M = n + R \tag{A9}$$

and

$$N = n \tag{A10}$$

Modal control law.- The coefficient matrices in equations (21a) and (21b) are, respectively,

$$A^{nn} = -\left[V^{nn}\Lambda^{nn^{-1}}H^{nn} + V^{nR}\Lambda^{RR^{-1}}H^{Rn}\right]\left[H_e{}^{nn}\right]^{-1} \tag{A11}$$

and

$$B^{nM} = \left[V^{nn} \quad \vdots \quad V^{nR}\right] \tag{A12}$$

Substituting these equations into equation (22) gives

$$X_{ss}^{n} = H_e{}^{nn}\left[V^{nn}\Lambda^{nn^{-1}}H^{nn} + V^{nR}\Lambda^{RR^{-1}}H^{Rn}\right]^{-1}\left[V^{nn}q^{n} + V^{nR}q^{R}\right] + Y^{n} \tag{A13}$$

and the expression for the actuator forces in equation (16) becomes

$$\alpha^{n} = \left[V^{nn}\Lambda^{nn^{-1}}H^{nn} + V^{nR}\Lambda^{RR^{-1}}H^{Rn}\right]^{-1}\left[V^{nn}q^{n} + V^{nR}q^{R}\right] \tag{A14}$$

Optimal control law.- For the case with $r = 0$, the coefficient matrices in equations (32a) and (32b) reduce, respectively, to

$$S^{nn} = -\left[U^{nn}\Lambda^{nn^{-1}}V^{nn}\Lambda^{nn^{-1}}H^{nn} + U^{nn}\Lambda^{nn^{-1}}V^{nR}\Lambda^{RR^{-1}}H^{Rn}\right] \tag{A15}$$

and

$$Z^{nM} = \left[U^{nn}\Lambda^{nn^{-1}}V^{nn} \quad \vdots \quad U^{nn}\Lambda^{nn^{-1}}V^{nR} \right] \tag{A16}$$

Rearranging and inverting matrix S^{nn} in equation (A15) yields

$$\left[S^{nn}\right]^{-1} = -\left[V^{nn}\Lambda^{nn^{-1}}H^{nn} + V^{nR}\Lambda^{RR^{-1}}H^{Rn}\right]^{-1}\Lambda^{nn^{-1}}U^{nn^{-1}} \tag{A17}$$

Solving for the state variables in equation (22) yields

$$X_{ss}^{n} = \left[V^{nn}\Lambda^{nn^{-1}}H^{nn} + V^{nR}\Lambda^{RR^{-1}}H^{Rn}\right]^{-1}\left[\Lambda^{nn}U^{nn^{-1}}\right]\left[U^{nn}\Lambda^{nn^{-1}}V^{nn}q^{n} + U^{nn}\Lambda^{nn^{-1}}V^{nR}q^{R}\right] + Y^{n} \tag{A18}$$

and by substituting equation (A18) into equation (16) with matrix $\left[H_e{}^{nn}\right]^{-1}$ as an identity matrix, the expression for the actuator forces is

$$\alpha_{ss}^{n} = \left[V^{nn}\Lambda^{nn^{-1}}H^{nn} + V^{nR}\Lambda^{RR^{-1}}H^{Rn}\right]^{-1}\left[V^{nn}q^{n} + V^{nR}q^{R}\right] \tag{A19}$$

which is the same expression as that in equation (A14). For this special case of an equal number of actuators and sensors, the actuator forces are independent of the matrix $\left[U_e{}^{NN}\right]^{-1}$. Using equations (13), (A9), and (A10) gives

$$\left[U_e{}^{nn}\right]^{-1}U^{nn} = V^{nn} \tag{A20}$$

$$\left[U_e{}^{nn}\right]^{-1}U^{nR} = V^{nR} \tag{A21}$$

and substituting equations (A20) and (A21) into equation (A19) yields

$$\alpha^n = \left[U^{nn}\Lambda^{nn^{-1}}H^{nn} + U^{nR}\Lambda^{RR^{-1}}H^{Rn}\right]^{-1}\left[U^{nn}q^n + U^{nR}q^R\right] \tag{A22}$$

REFERENCES

1. Anon.: Active Optical System for Spaceborne Telescopes. Eng. Rep. No. 8525 (Contract No. NAS 1-5198), Electro-Optical Group, Perkin-Elmer Corp., Oct. 14, 1966. (Available as NASA CR-66297.)
2. Creedon, J. F.; and Lindgren, A. G.: Control of the Optical Surface of a Thin, Deformable Primary Mirror With Application to an Orbiting Astronomical Observatory. Automatica, vol. 6, no. 5, Sept. 1970, pp. 643-660.
3. Howell, W. E.; and Creedon, J. F.: A Technique for Designing Active Control Systems for Astronomical-Telescope Mirrors. NASA TN D-7090, 1973.
4. Robertson, Hugh J.: Evaluation of the Thin Deformable Active Optics Mirror Concept. NASA CR-2073, 1972.
5. Robertson, Hugh J.: Development of an Active Optics Concept Using a Thin Deformable Mirror. NASA CR-1593, 1970.
6. MacNeal, Richard H., ed.: The NASTRAN Theoretical Manual. NASA SP-221, 1970.
7. Ostroff, Aaron J.; and McCann, Mary: Analysis of the Dynamics of Thin Primary Mirrors for Large Astronomical Telescopes. NASA TM X-2790, 1973.
8. Ogata, Katsuhiko: State Space Analysis of Control Systems. Prentice-Hall, Inc., c.1967.
9. Biggs, John M.: Introduction to Structural Dynamics. McGraw-Hill Book Co., Inc., c.1964.
10. Conte, S. D.: Elementary Numerical Analysis. McGraw-Hill Book Co., Inc., c.1965.

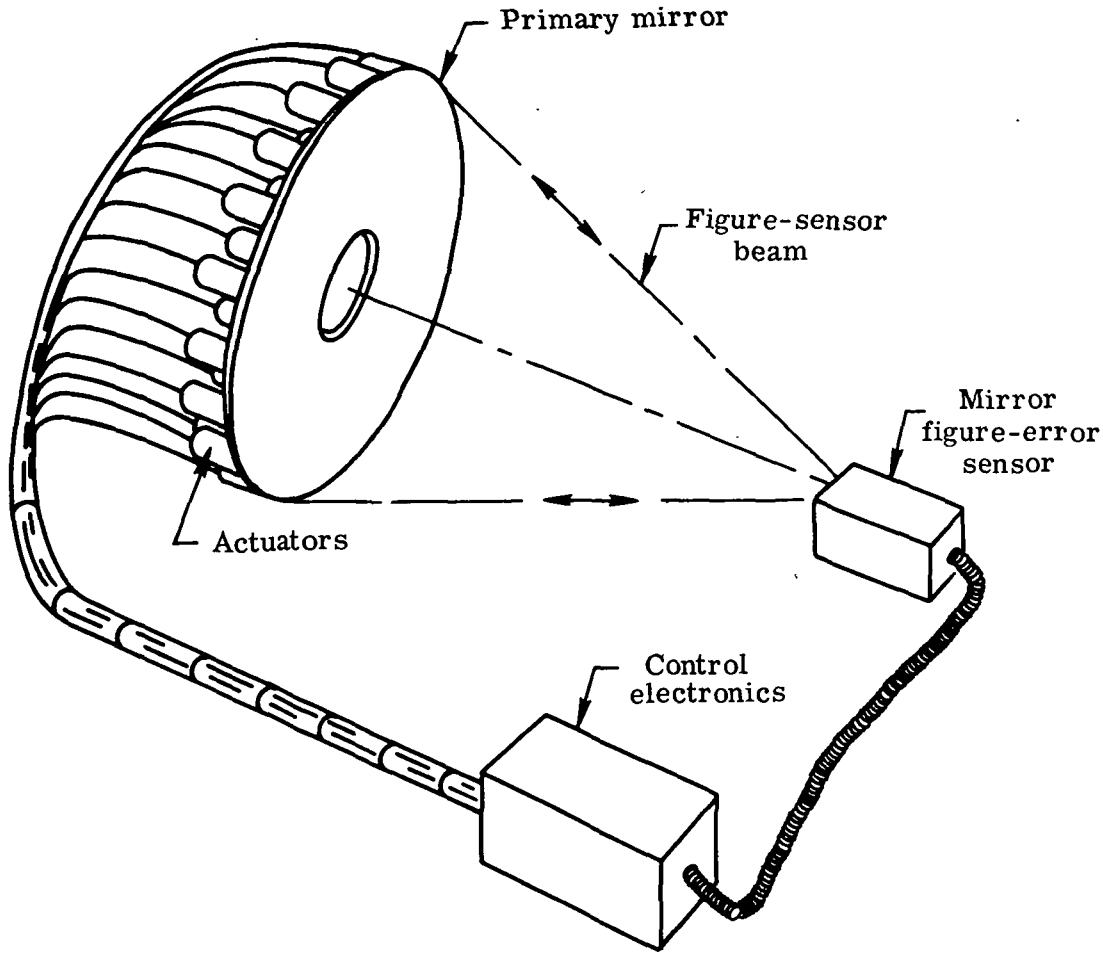

Figure 1.- Schematic diagram of the deformable-mirror active-optics concept.

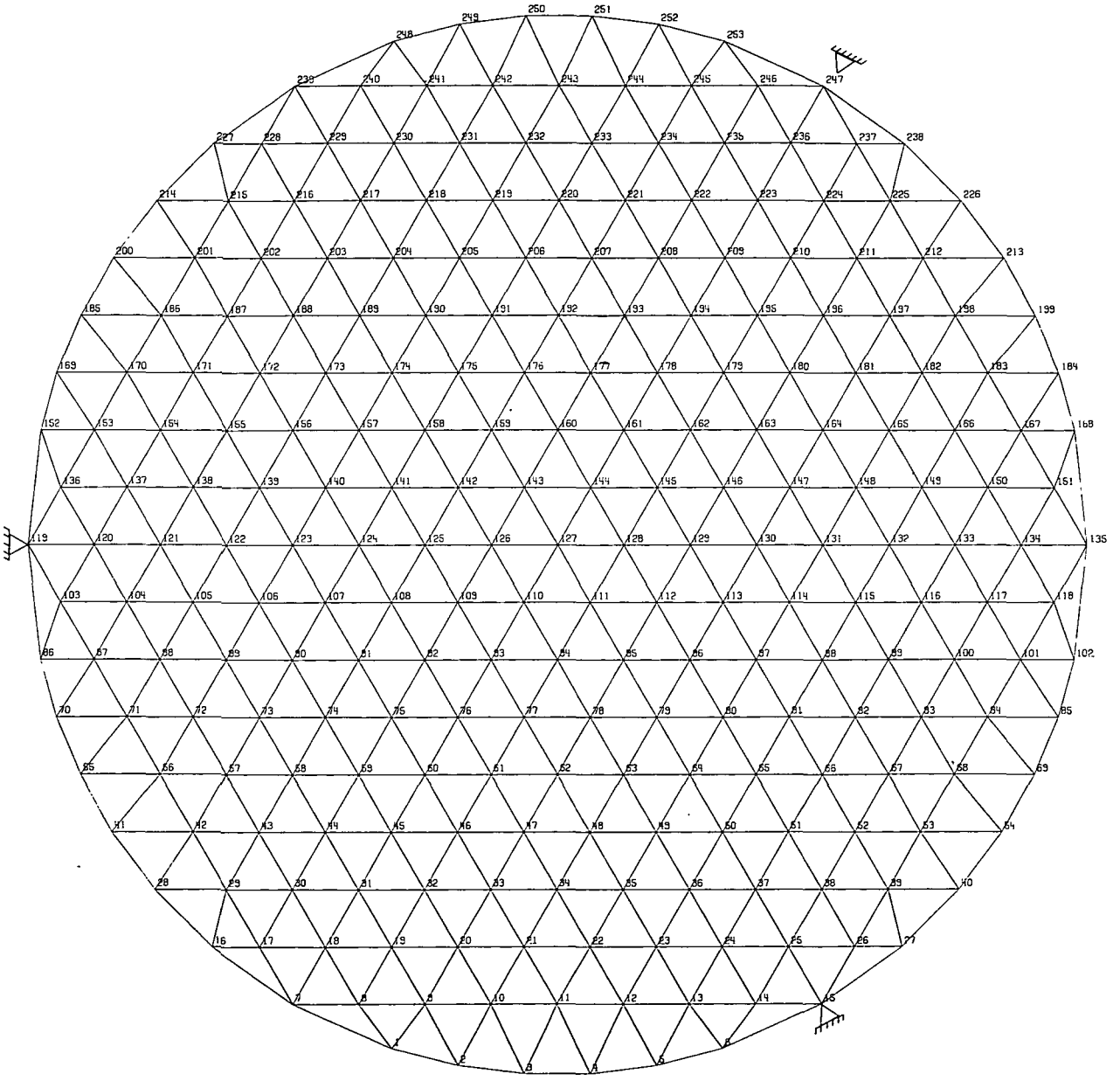

Figure 2.- Finite-element structural model.

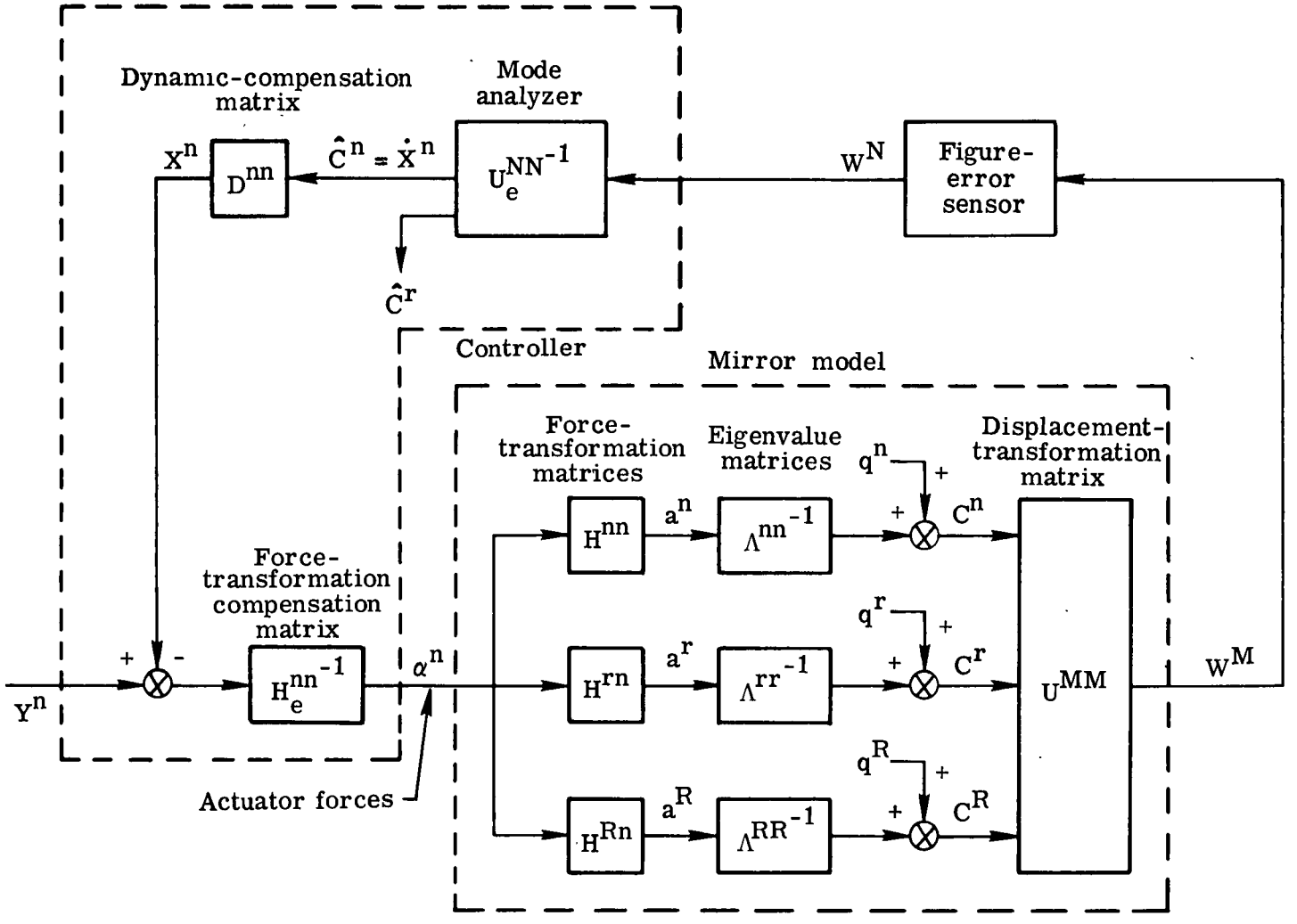

Figure 3.- Block diagram of modal control loop.

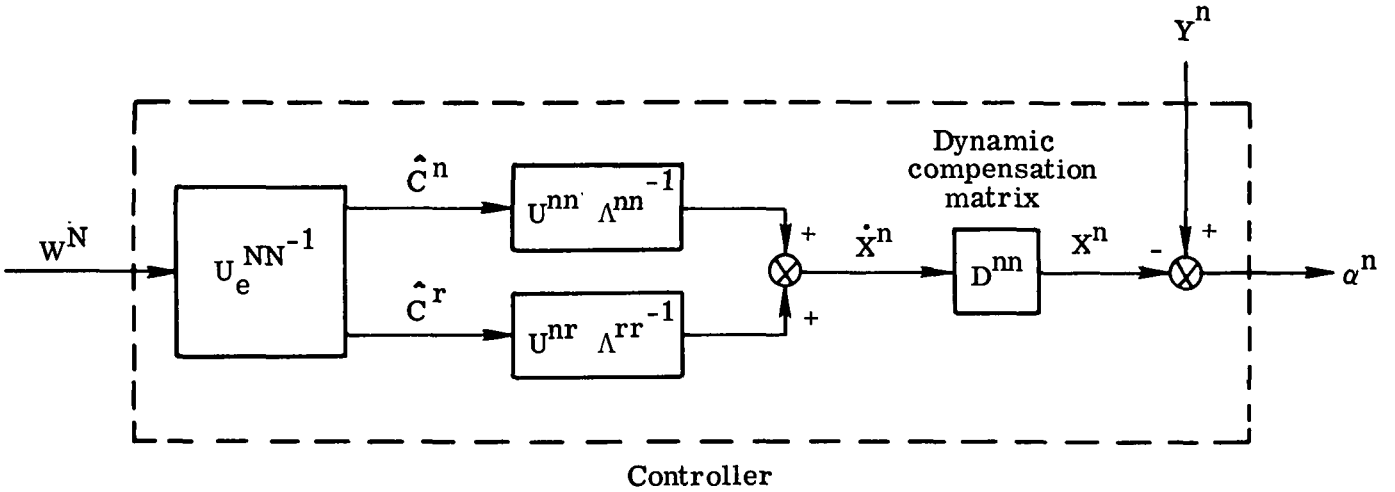

Figure 4.- Block diagram of least-squares optimal controller.

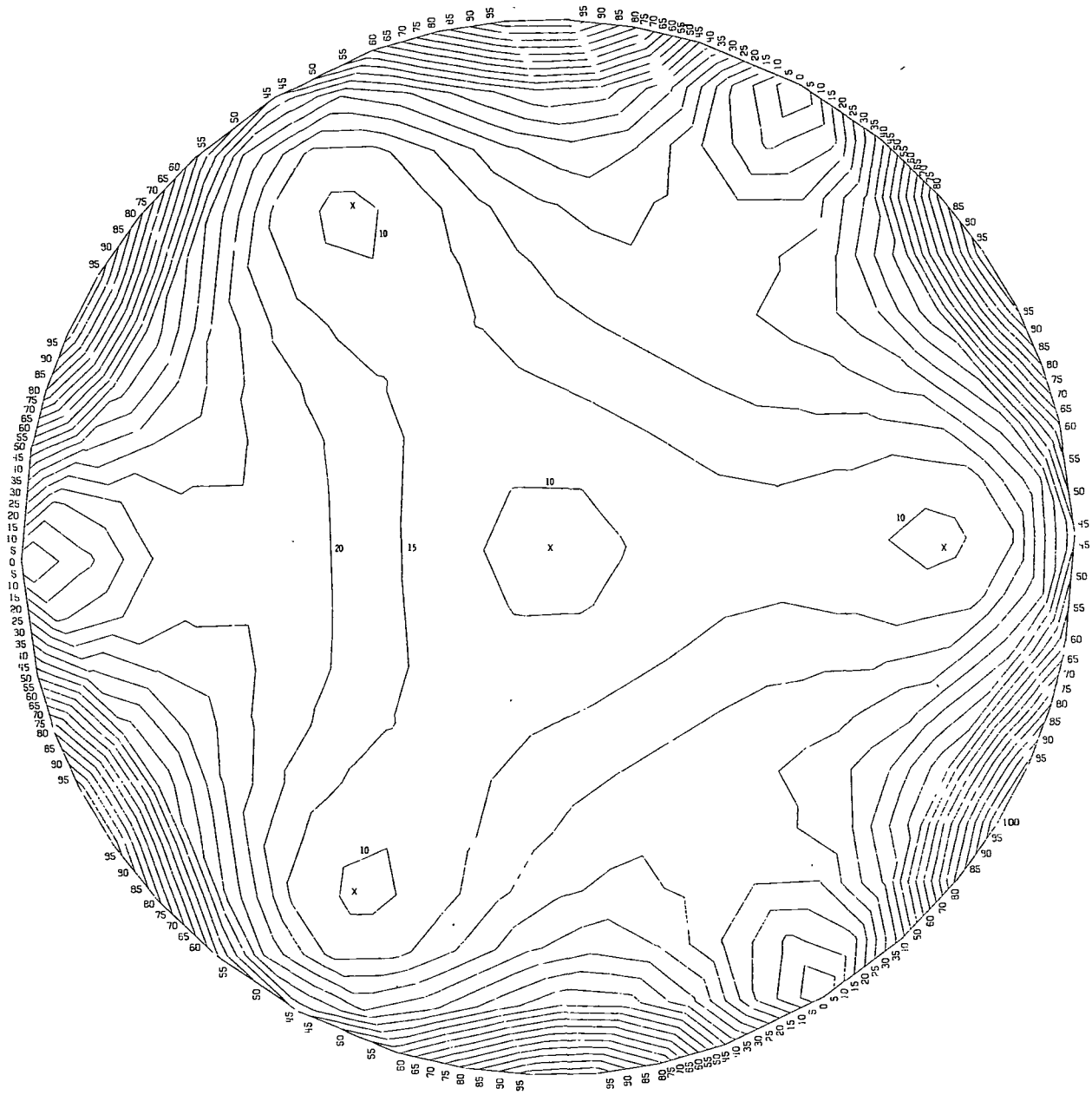

(a) Four actuators.

Figure 5.- Contour maps of diagonal elements of flexibility matrix of uncontrolled modes.

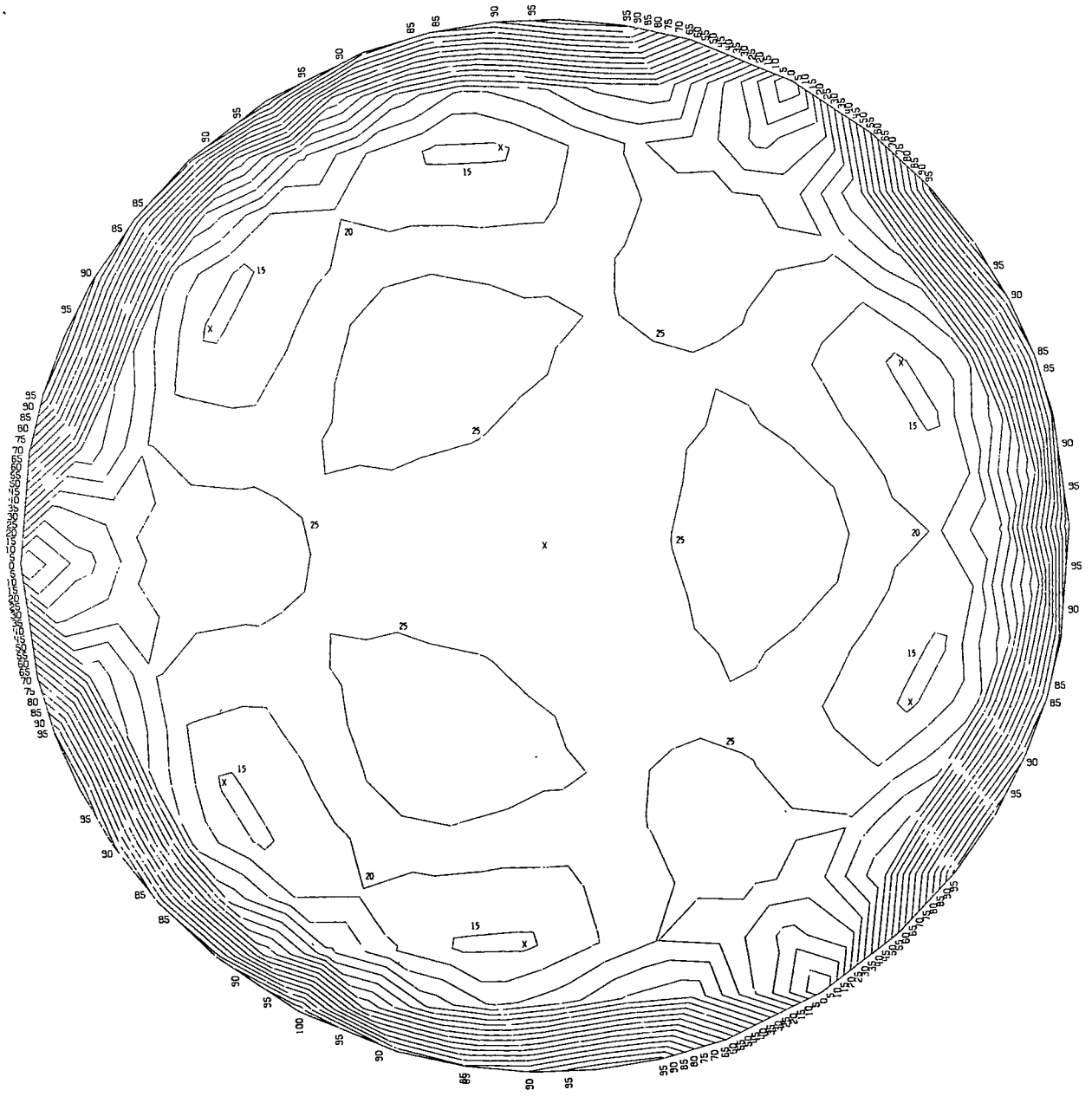

(b) Seven actuators.

Figure 5.- Continued.

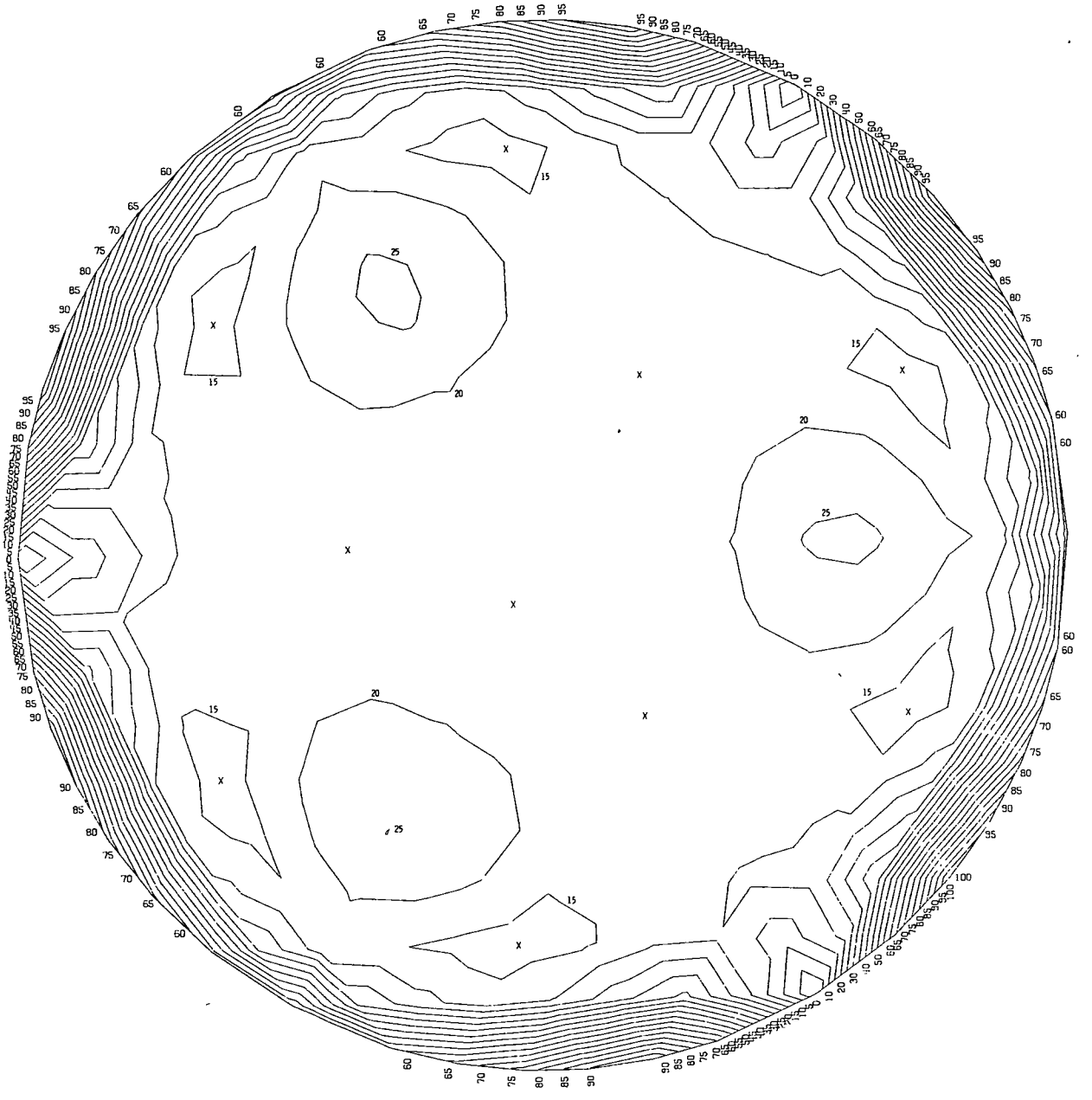

(c) Ten actuators.

Figure 5.- Continued.

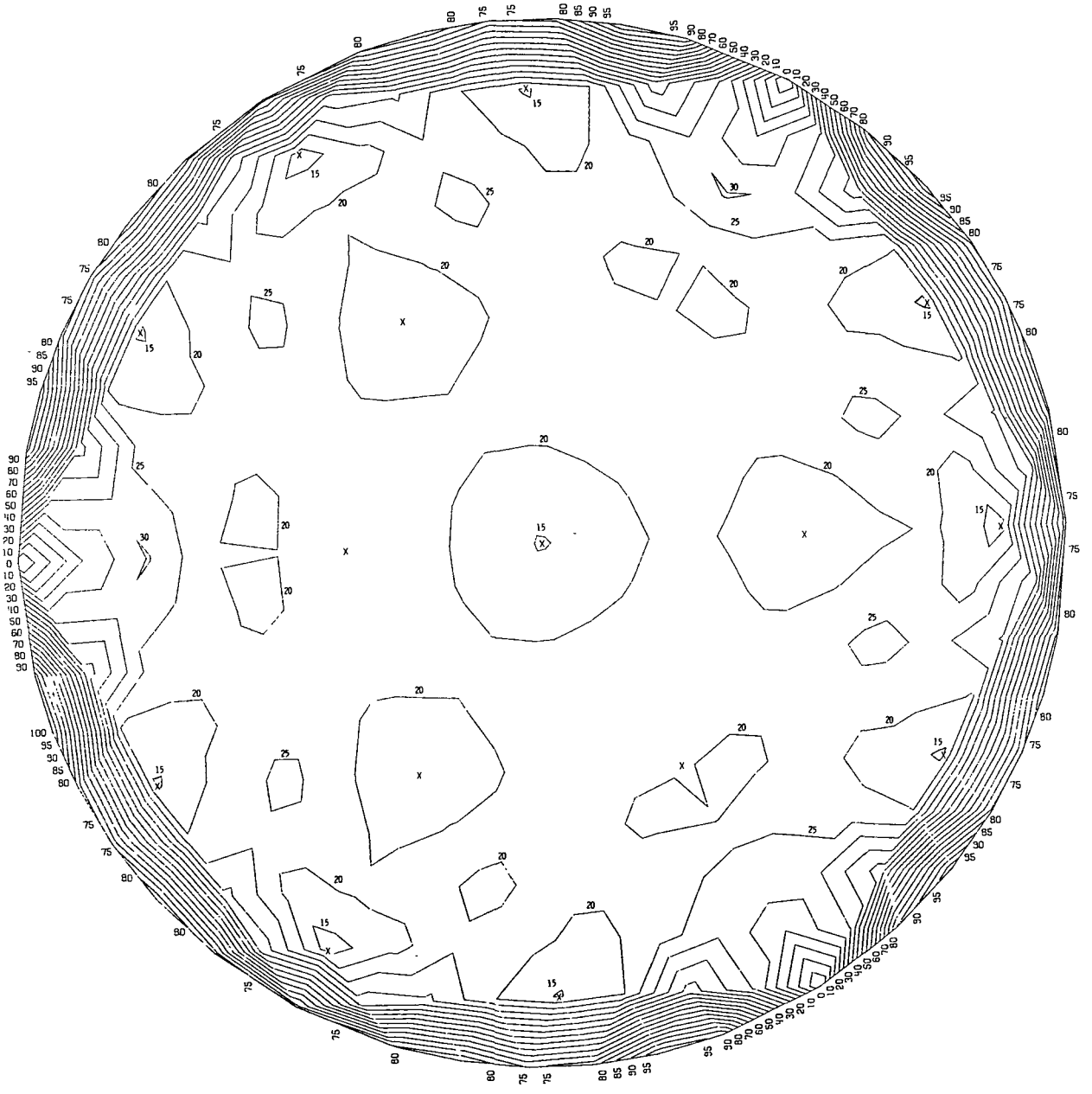

(d) Fifteen actuators.

Figure 5.- Continued.

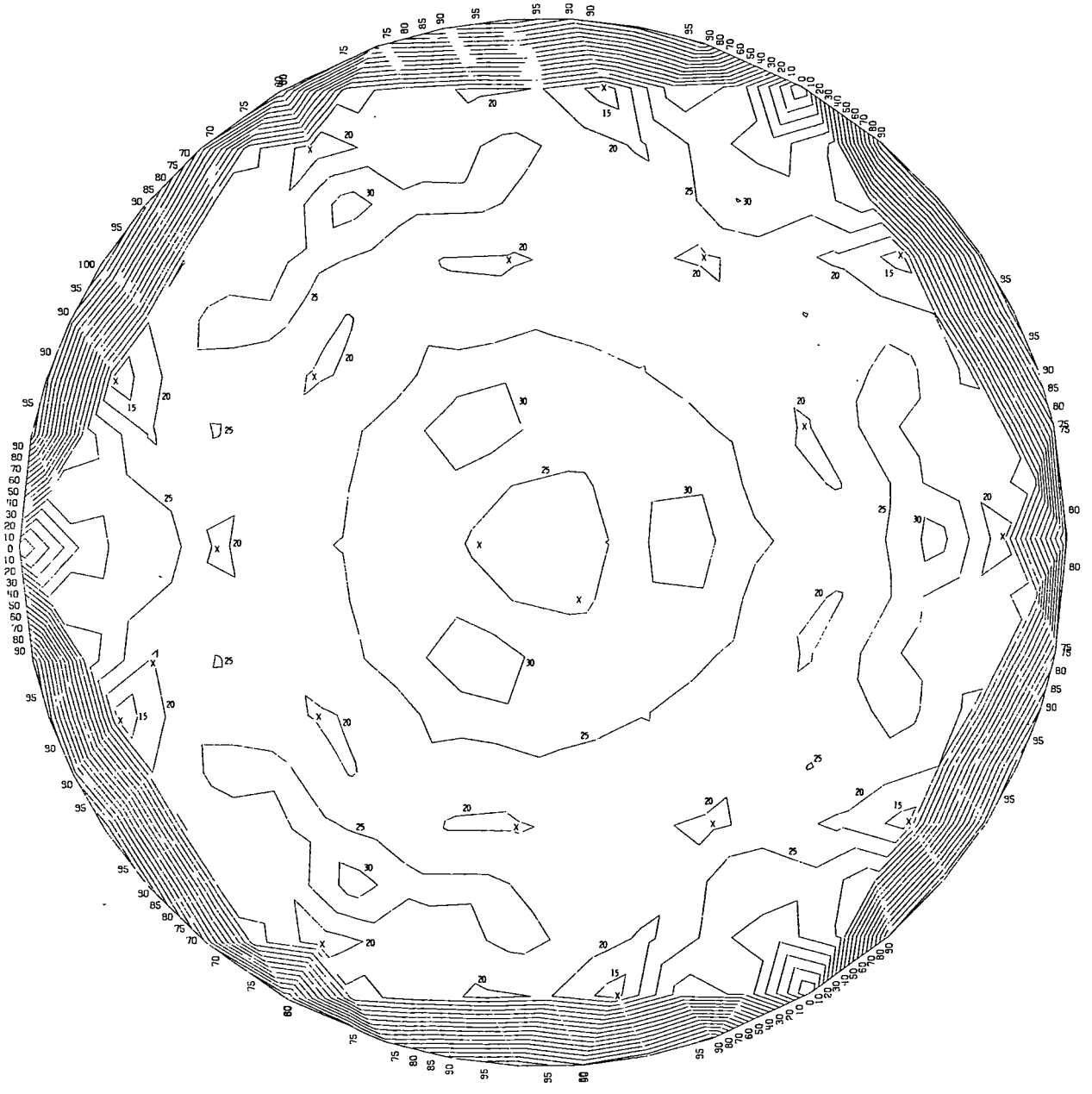

(e) Twenty actuators.

Figure 5.- Concluded.

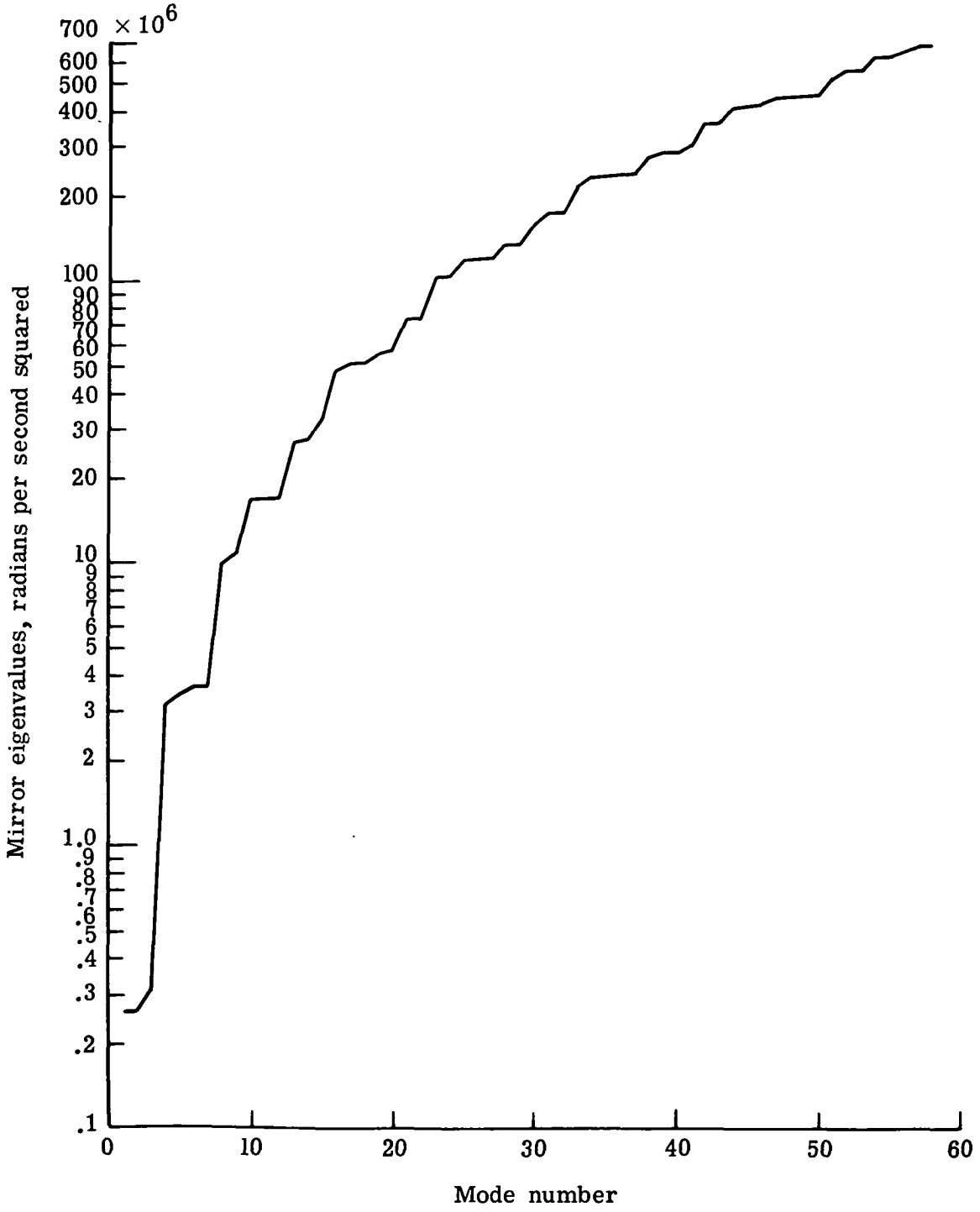

Figure 6.- Eigenvalues for first 58 modes for 0.762-meter-diameter mirror with a 60-to-1 diameter-to-thickness ratio and a radius of curvature of 4.5212 meters.

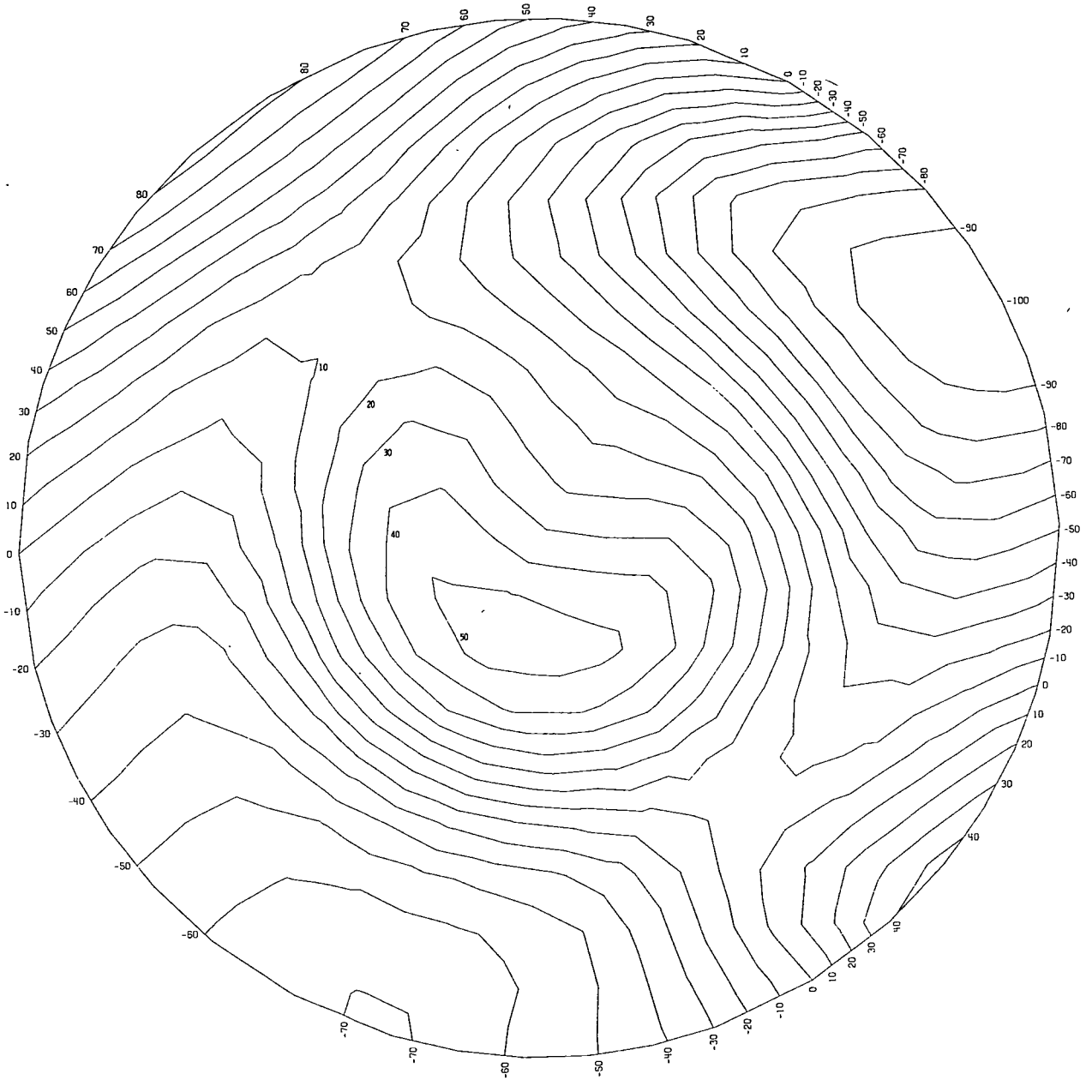

(a) Error distribution 1.

Figure 7.- Contour maps of three error distributions.

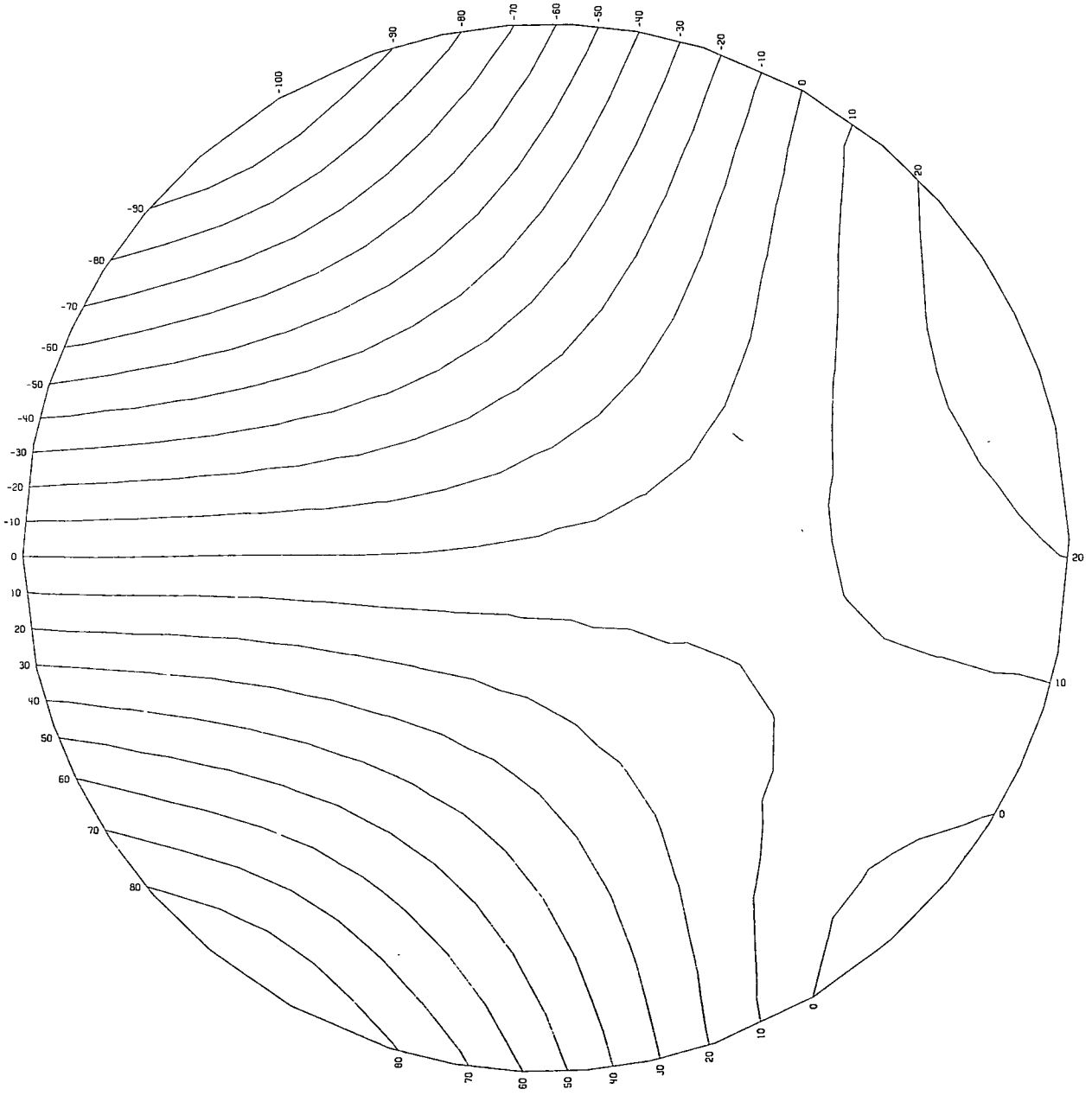

(b) Error distribution 2.

Figure 7.- Continued.

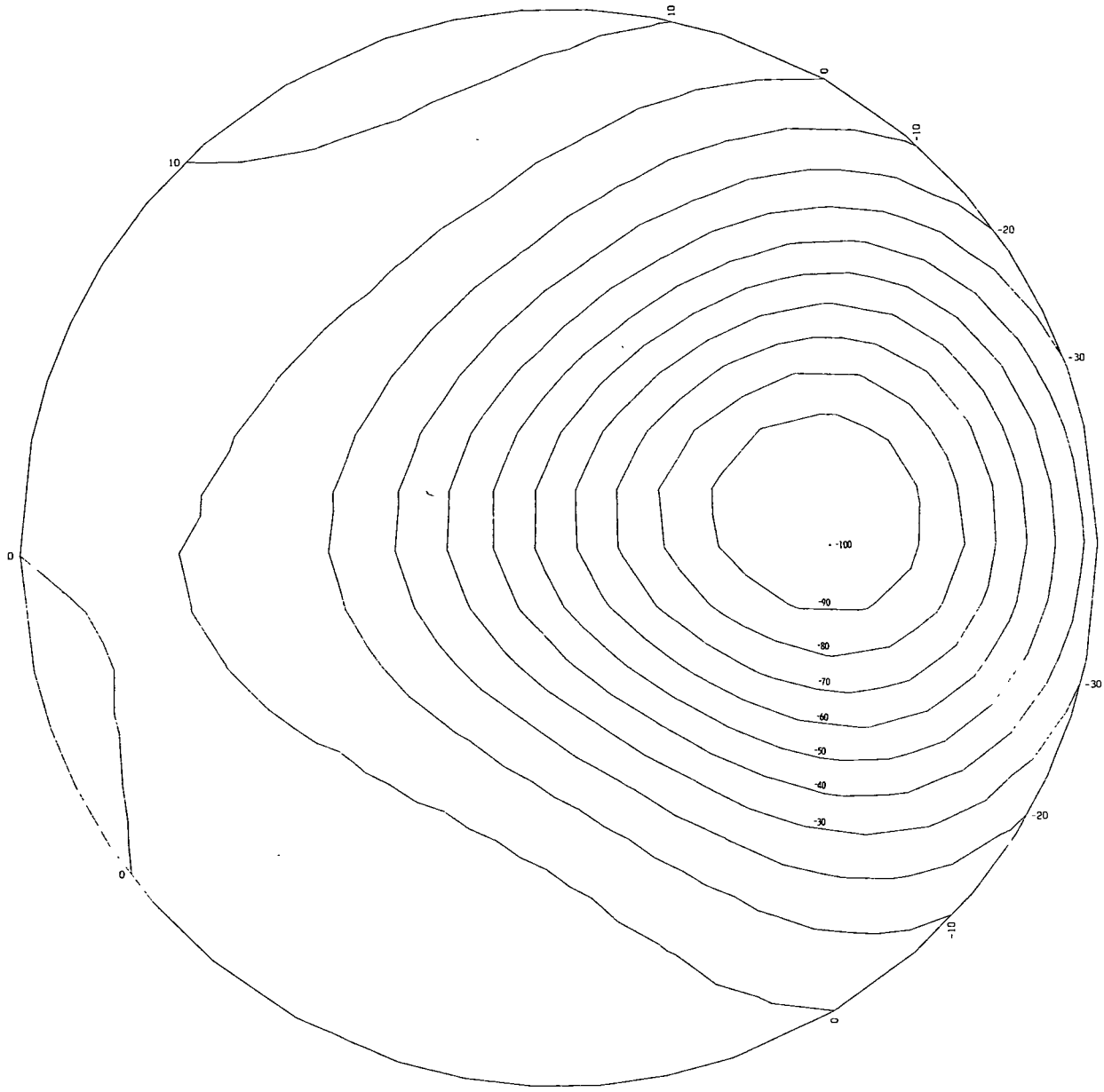

(c) Error distribution 3.

Figure 7.- Concluded.

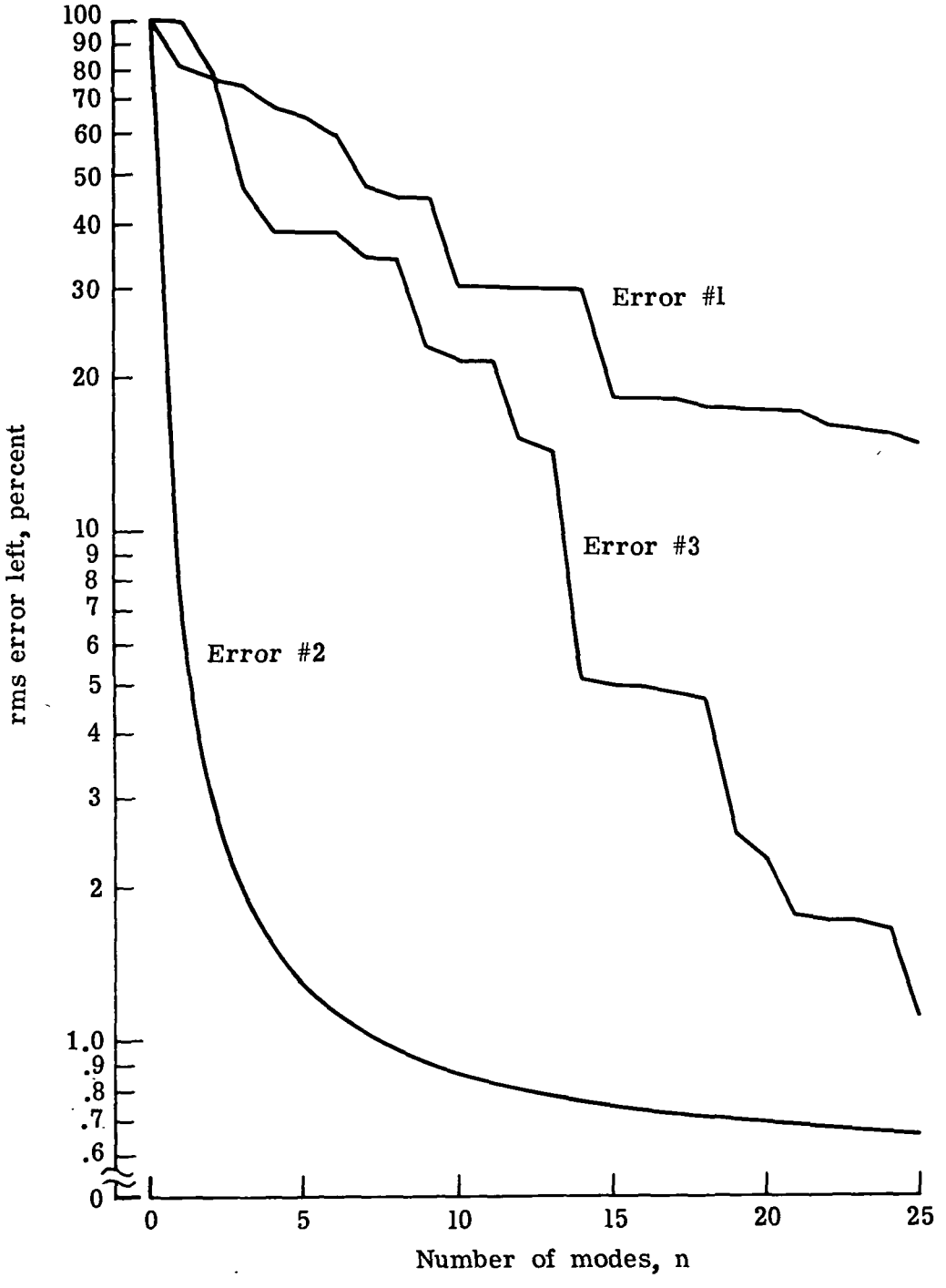

Figure 8.- Percent of rms error left after deleting the n controlled modes for the three error distributions.

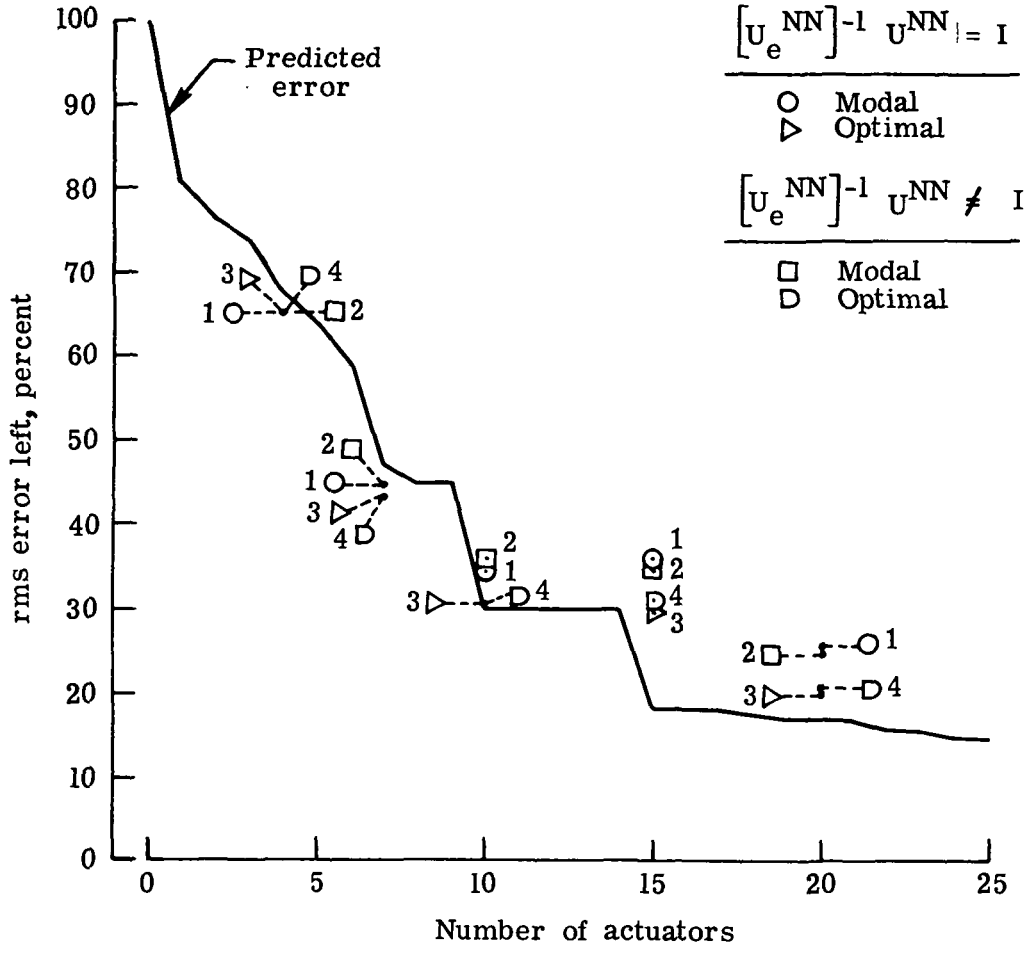

Figure 9.- Percent of rms error left as a function of number of actuators for error number 1 with a perfect figure-error sensor.

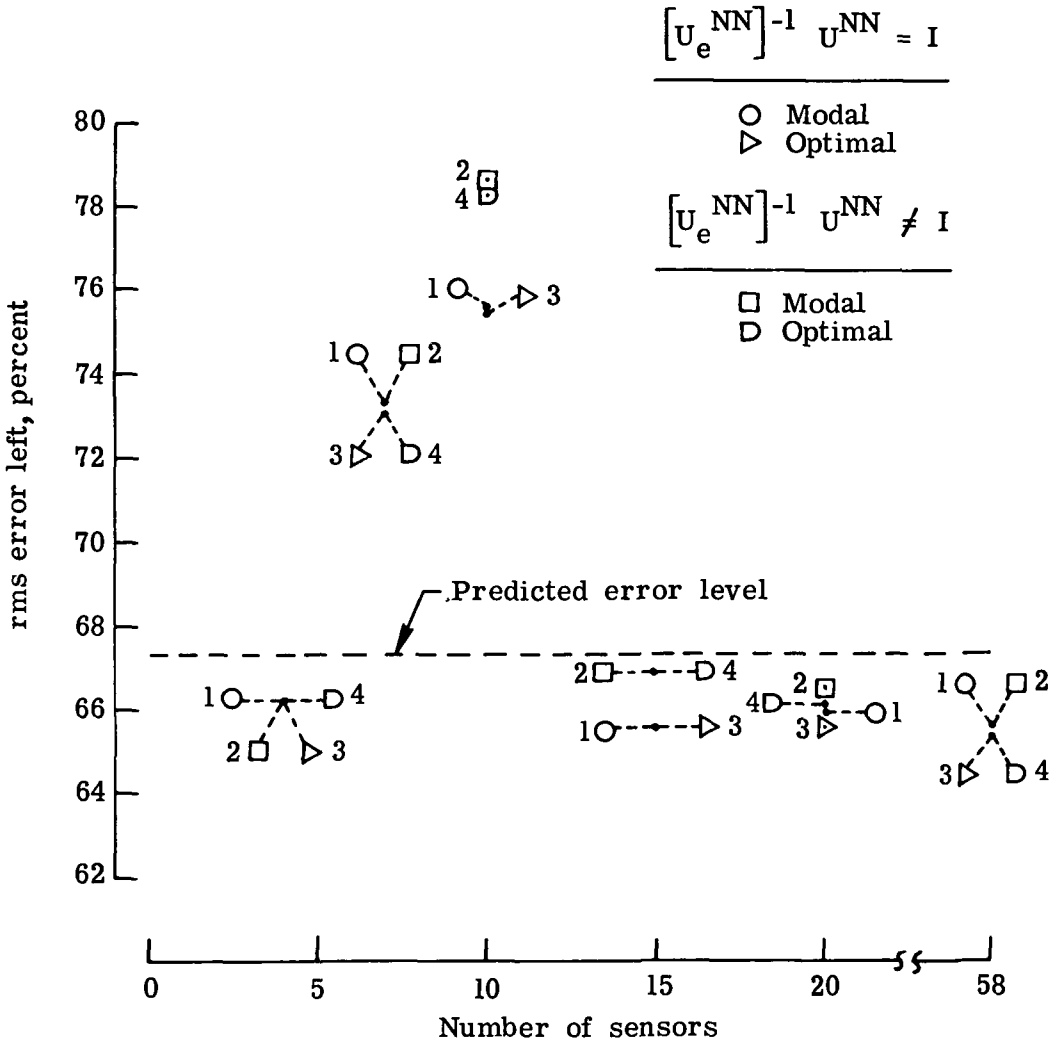

Figure 10.- Percent of rms error left as a function of number of sensors for four actuators and error number 1.

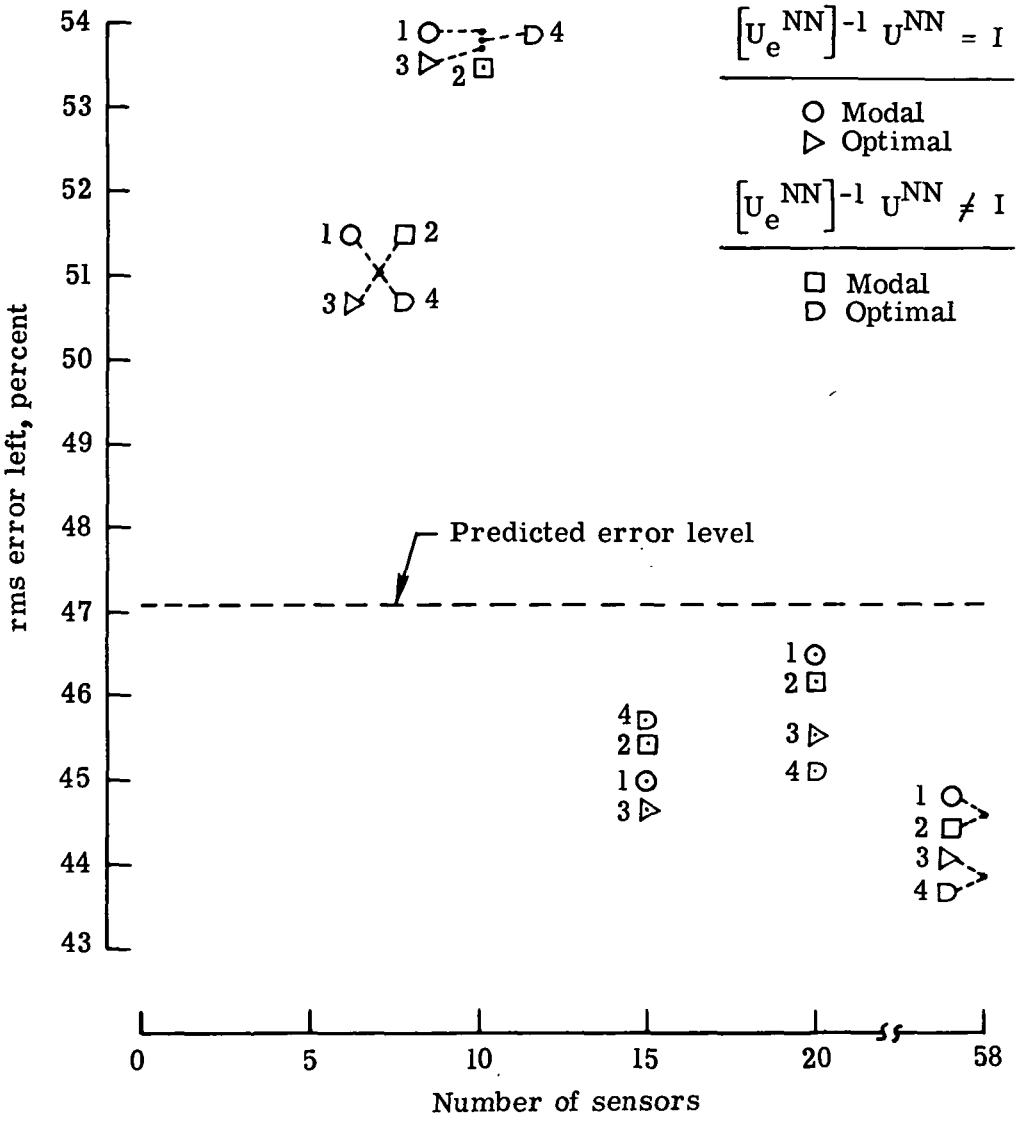

Figure 11.- Percent of rms error left as a function of number of sensors for seven actuators and error number 1.

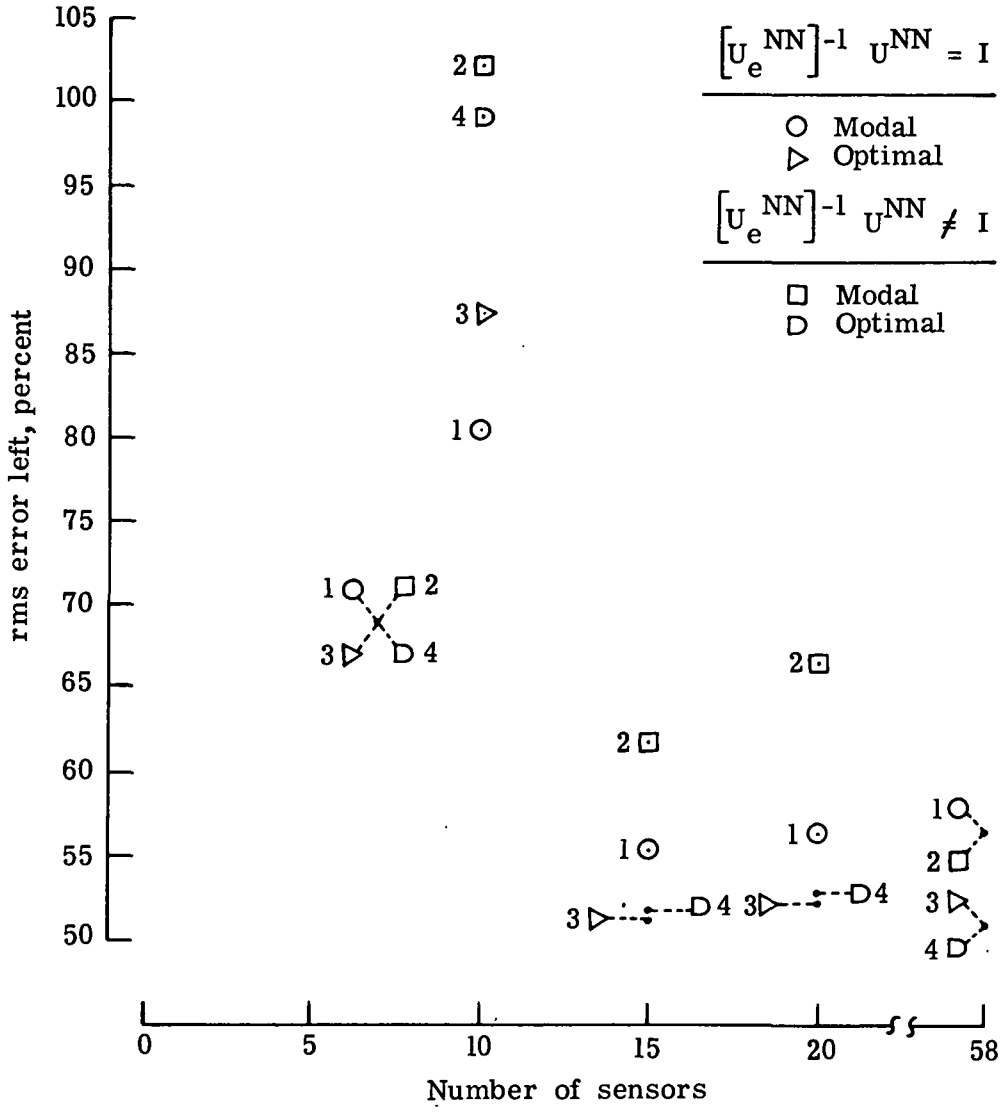

Figure 12.- Percent of rms error left as a function of number of sensors for seven actuators and error number 1 for a bad actuator location.

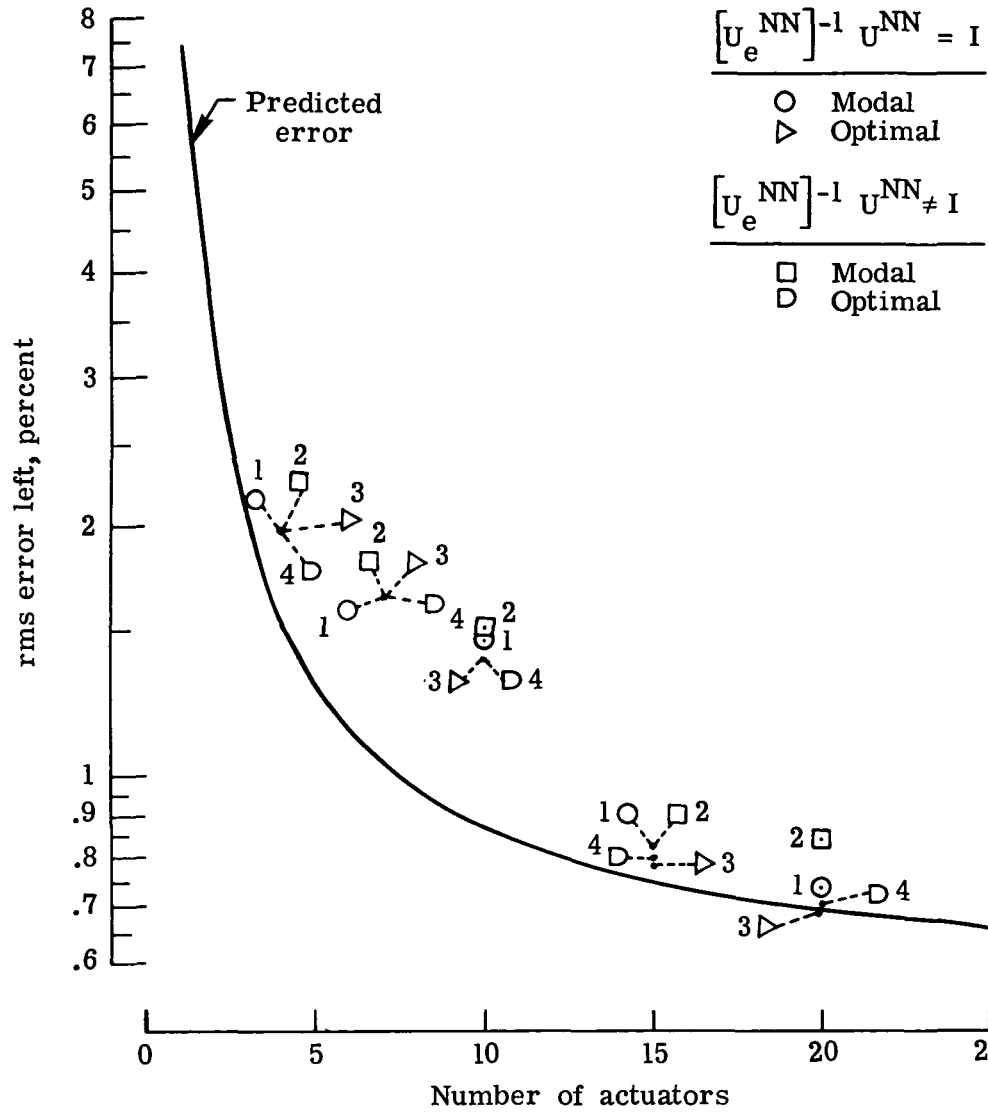

Figure 13.- Percent of rms error left as a function of number of actuators for error number 2 and a perfect figure sensor.

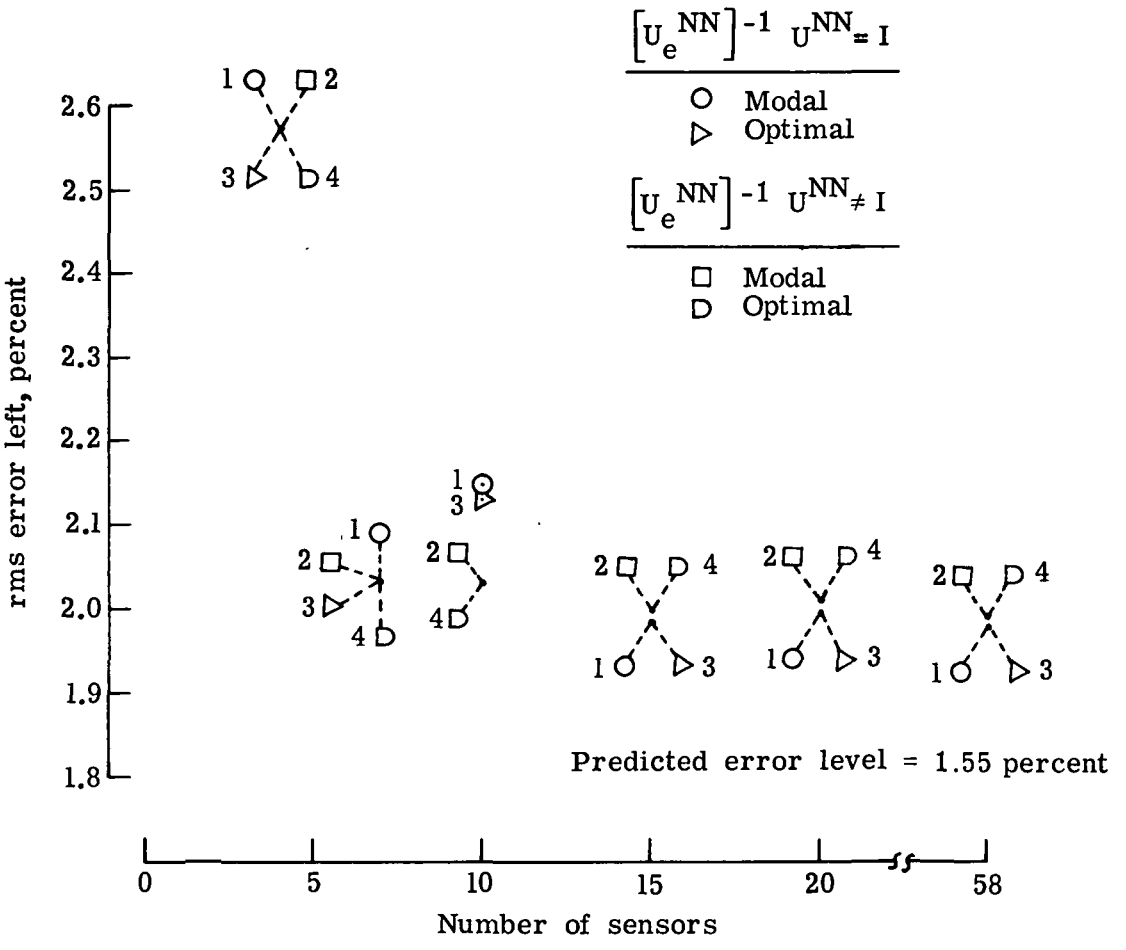

Figure 14.- Percent of rms error left as a function of number of sensors for four actuators and error number 2.

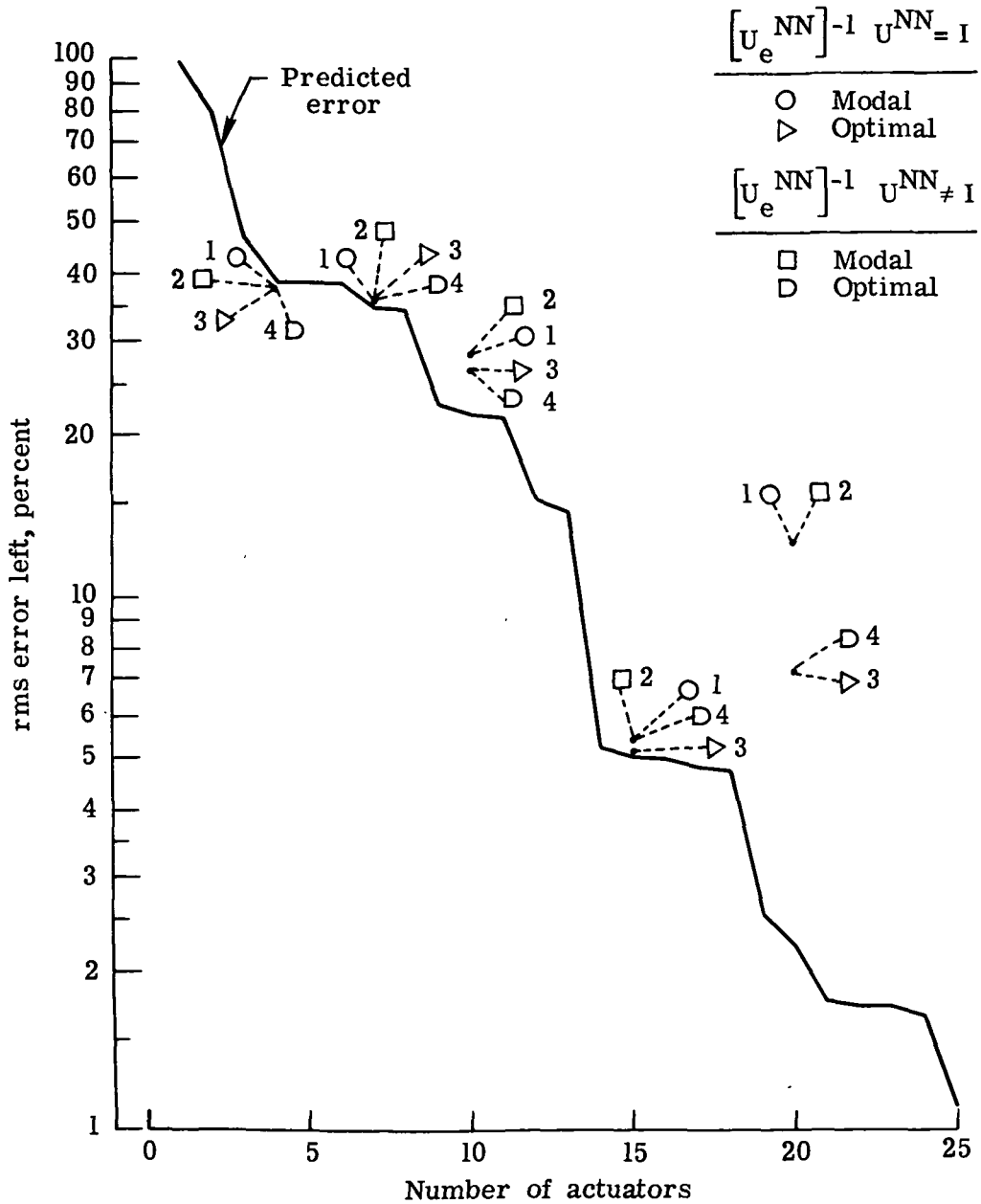

Figure 15.- Percent of rms error left as a function of number of actuators for error number 3 and a perfect figure sensor.

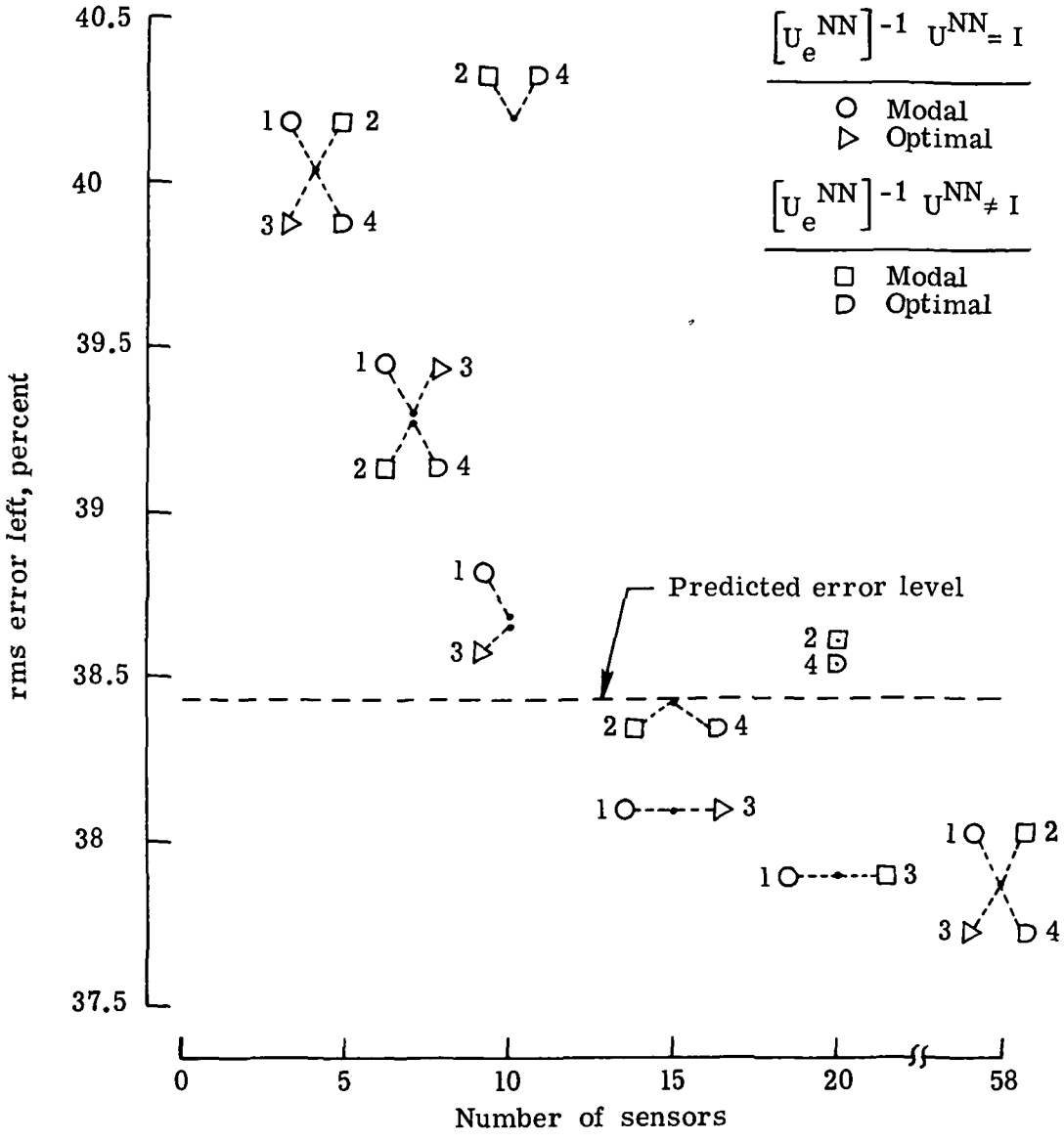

Figure 16.- Percent of rms error left as a function of number of sensors for four actuators and error number 3.

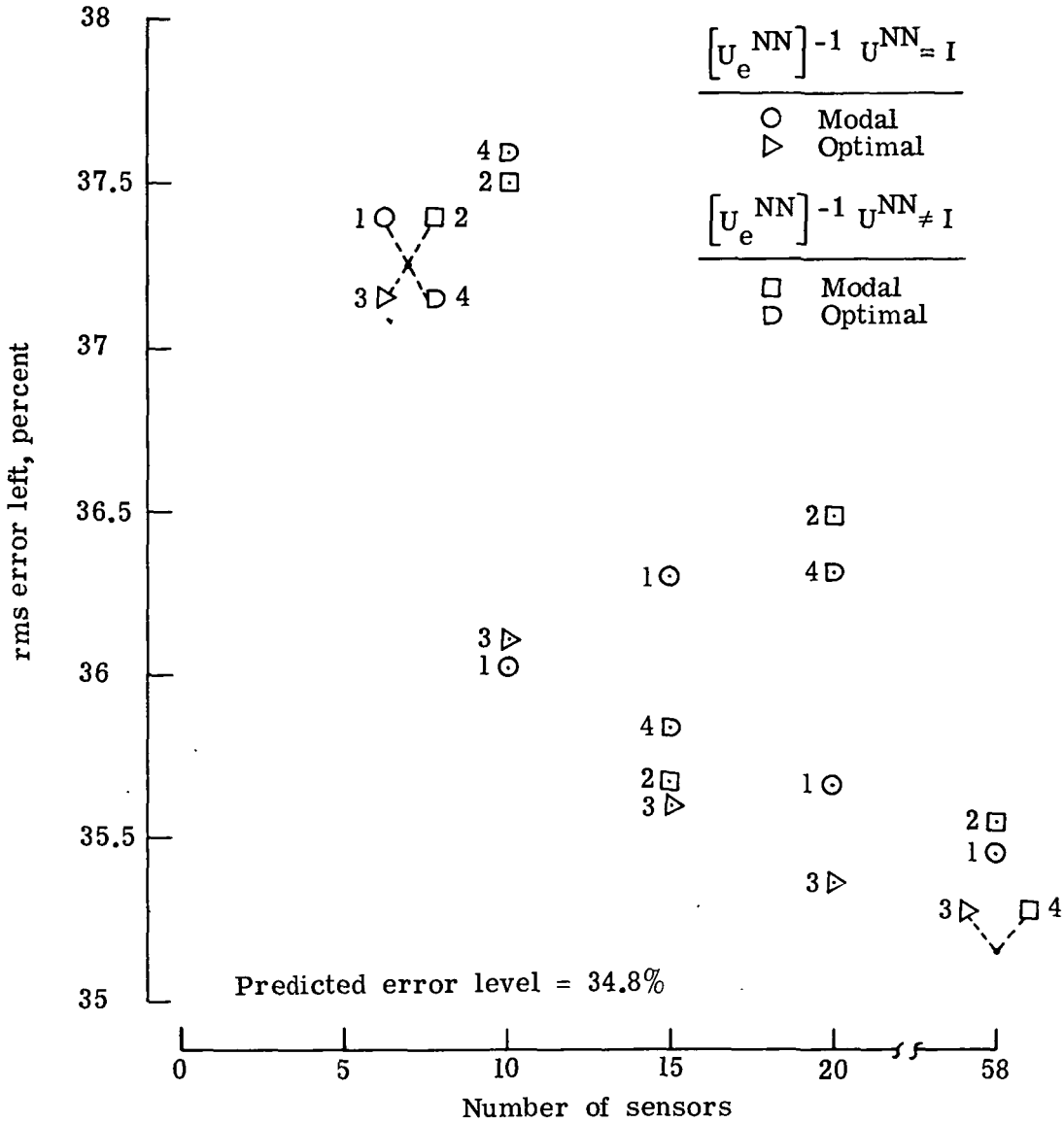

Figure 17.- Percent of rms error left as a function of number of sensors for seven actuators and error number 3.

NASA-Langley, 1973 —— 10 L-8862

NATIONAL AERONAUTICS AND SPACE ADMINISTRATION
WASHINGTON, D.C. 20546

OFFICIAL BUSINESS
PENALTY FOR PRIVATE USE $300

SPECIAL FOURTH-CLASS RATE
BOOK

POSTAGE AND FEES PAID
NATIONAL AERONAUTICS AND
SPACE ADMINISTRATION
451

U.S.MAIL

POSTMASTER: If Undeliverable (Section 158 Postal Manual) Do Not Return

"The aeronautical and space activities of the United States shall be conducted so as to contribute . . . to the expansion of human knowledge of phenomena in the atmosphere and space. The Administration shall provide for the widest practicable and appropriate dissemination of information concerning its activities and the results thereof."

—NATIONAL AERONAUTICS AND SPACE ACT OF 1958

NASA SCIENTIFIC AND TECHNICAL PUBLICATIONS

TECHNICAL REPORTS: Scientific and technical information considered important, complete, and a lasting contribution to existing knowledge.

TECHNICAL NOTES: Information less broad in scope but nevertheless of importance as a contribution to existing knowledge.

TECHNICAL MEMORANDUMS: Information receiving limited distribution because of preliminary data, security classification, or other reasons. Also includes conference proceedings with either limited or unlimited distribution.

CONTRACTOR REPORTS: Scientific and technical information generated under a NASA contract or grant and considered an important contribution to existing knowledge.

TECHNICAL TRANSLATIONS: Information published in a foreign language considered to merit NASA distribution in English.

SPECIAL PUBLICATIONS: Information derived from or of value to NASA activities. Publications include final reports of major projects, monographs, data compilations, handbooks, sourcebooks, and special bibliographies.

TECHNOLOGY UTILIZATION PUBLICATIONS: Information on technology used by NASA that may be of particular interest in commercial and other non-aerospace applications. Publications include Tech Briefs, Technology Utilization Reports and Technology Surveys.

Details on the availability of these publications may be obtained from:

SCIENTIFIC AND TECHNICAL INFORMATION OFFICE

NATIONAL AERONAUTICS AND SPACE ADMINISTRATION

Washington, D.C. 20546